ALPHA FOUNDATION FOR THE IMPROVEMENT OF MINE SAFETY AND HEALTH

Final Technical Report

Project Title: Numerical Modeling of Overburden and Pillar Mechanics for Determination of Global Ground Stability in Underground Coal Mines

Grant Number: AFC719-67

Organization: Colorado School of Mines

Principal Investigator: Gabriel Walton, Assistant Professor

Contact Information : Gabriel Walton, Principal Investigator
Center for Underground Construction & Tunneling
Phone: (303) 384-2235
gwalton@mines.edu

Period of Performance: 09/01/2018 – 02/29/2020

Acknowledgement/Disclaimer

This study was sponsored by the Alpha Foundation for the Improvement of Mine Safety and Health, Inc. (ALPHA FOUNDATION). The views, opinions and recommendations expressed herein are solely those of the authors and do not imply any endorsement by the ALPHA FOUNDATION, its Directors and staff.

List of Abbreviations

ARBS: Analysis of Roof Bolt Systems
BLR: Binary Logistic Regression
BS: Black Shale
BT: Bedding Thickness
CMRR: Coal Mine Roof Rating
CY: Continuously Yielding joint
DEM: Discrete Element Method
DFN: Discrete fracture Network
EBP: Elastic-Brittle-Plastic
FLAC^{3D}: Fast Langrangian Analysis of Continua in three-dimension
FoS: Factor of Safety
LBP and RBP: Left and Right Barrier Pillar
LS: Limestone
MB: Mark-Bieniawski pillar strength equation
OB: Overburden
SS: Sandstone
SUBI: Strain-Softening Ubiquitous Joint constitutive model
TAT: Tributary Area Theory
UDEC: Universal Distinct Element Code
W/H: Width to Height ratio
YS: Yield Strength
CHILE: Continuous, Homogeneous, Isotropic, Linearly Elastic material properties

List of Symbols:

ϵ^{ps}: Critical plastic shear strain
φi: Initial friction angle
φ: Intrinsic friction angle
φ_r: Residual friction angle of matrix in SUBI model
ψ: Dilation angle
σ_s: Pillar strength
ν_{12}: Characterizes lateral contraction in the plane of isotropy when tension is applied in this plane in transversely isotropic model
ν_{13} and ν_{23}: Characterizes lateral contraction in the plane of isotropy when tension is applied in the direction normal to it in a transversely isotropic model
σ_{yy} or σ_v: Stress in the y direction (vertical)
γ: Unit weight
β: Abutment angle
$ARBS_G$: Empirically suggested ARBS value
Cr: Residual cohesion of matrix in SUBI model
E: Young's modulus
E_1 and E_2: Modulus in plane of isotropy in transversely isotropic model
E_3: Modulus in plane perpendicular to the plane of isotropy in transversely isotropic model

E_{rm}: Rockmass modulus
G: Shear modulus
G_{13} and G_{23}: Cross shear modulus in transversely isotropic model
H: Mining depth
W_{panel}: Width of panel
W_{pillar}: Width of pillar
jφi: Initial joint friction angle in SUBI model
jci: Joint cohesion in SUBI model
jdil: Joint dilation angle in SUBI model
jkn: Joint normal stiffness
jks: Joint shear stiffness
jen: Exponent of joint elastic normal stiffness
jes: Exponent of joint elastic shear stiffness
jt: Joint tension in SUBI model
k_o: ratio of horizontal to vertical stress
K: Bulk modulus
S_{max}: Maximum subsidence
Tr: Residual tensile strength of matrix in SUBI model

1.0 Executive Summary

Global underground failure in a US coal mine has not occurred since 2006, and injuries and fatalities from local fall of ground continue to decrease over time thanks to wide-spread implementation of empirical and analytical methods. However, the mechanics governing these complex systems remain poorly understood. Existing empirical and analytical methods for engineering design in underground coal mines are typically considered conservative, and therefore, safe. However, if the assumptions or observations these methods are based on do not represent the in-situ conditions, even supposedly conservative approaches will not ensure safety.

Previous research has suggested that the issue of global ground stability is a composite problem that should account for both overburden and pillar behavior. Failure to account for the interaction between system components could lead to catastrophic mine failure as observed in the cases of the Crandall Canyon and Coalbrook mine disasters. There is, therefore, a pressing need to investigate the interdependence of the pillars and overburden and to identify critical parameters that have historically been ignored in pillar design methodologies.

The Alpha Foundation identified five key research questions related to this topic, all of which are addressed herein. Investigating roof stability and its purported self-supporting capacity will provide insight into the impact that roof conditions such as intact material and discontinuity properties, heterogeneities, constitutive models, in-situ stress ratios, mining depths, and DFN properties have on roof stability and pillar stress. This study addresses the shortcomings of current state-of-practice by using numerical models to enhance the mechanical understanding of the interaction between the overburden and pillars.

A methodical approach was implemented, increasing complexity while relating numerical model results to existing empirical and analytical approaches to confirm realistic behavior. The critical inputs governing roof stability and the calibrated coal pillar constitutive model were combined in single-entry and panel scale models. Panel-scale models introduced heterogenous stratigraphies, various pillar properties, and simulated both in and out of plane depillaring. Both production and barrier pillar stresses, as well as local entry stability, and propagation of yield were monitored to identify critical failure mechanisms.

The findings of this study identify key considerations for analyzing roof stability, roof support design, and pillar design that account for overburden material properties and other pertinent geomining conditions. The model inputs significantly controlling roof stability include depth and intact material type, particularly the presence of small-scale planes of weakness (i.e. between major beds); as depth increases, other inputs such as horizontal stress ratio, presence of sub-vertical jointing, and bedding thickness all become more significant controls on roof stability. Furthermore, TAT and MB are shown to provide inaccurate results, with TAT tending to overestimate pillar loads and MB overestimating pillar strength. The question of "which element yields first in a global mine failure, the pillars or the overburden?", is answered based on the unique loading conditions studied herein. The findings indicate that at the mine-scale yield initiates in the overburden, but global mine failure initiates in the pillars.

This grant from the Alpha Foundation produced 2 conference papers and 2 journal articles, and funded 2 presentations at academic conferences. The research presented herein will impact the future of mining health and safety by advancing the state of practice of roof support and pillar design to account for overburden mechanical properties. Implementation of the design considerations presented herein have the benefit of making underground mining safer, with the ultimate goal of zero injuries and fatalities.

2.0 Problem Statement & Objective

The current state-of-practice for designing underground workings in mining applications relies heavily on simplifying assumptions regarding the mechanical behavior of rocks and rockmasses. In particular, the mechanical interaction between roof, floor, and support (i.e. pillars, liners, bolts, etc.) is poorly understood due to isolation of these interdependent systems in both research and design applications (Reed et al., 2016). Conventional pillar design assumes that the overburden has no self-supporting capacity, which is generally invalid. The study documented in this report addresses the research questions raised in the Alpha Foundation proposal solicitation under the topic *"Understanding the Role of Overburden Mechanics in Pillar Design and Global Ground Stability"*.

Although a catastrophic global (i.e. total) underground failure has not occurred in the United States of America (USA) since the Crandall Canyon mine disaster in 2006, and mine fatalities have steadily decreased since 1990, roof and pillar failures still kill and injure miners every year (Mark et al., 2011). Improving our understanding of mechanical interaction in the subsurface will help reduce the negative impacts to health, human safety, and productivity that affect underground workings. Analytical and empirical methods for roof and pillar stability evaluation (e.g. Evans, 1941; Molinda and Mark, 1993; Mark et al., 2005; Mark, 2015) have been developed and are major components in current industry-standard practices for ground-control. However, despite the large and diverse body of research regarding ground control, ground falls accounted for 112 fatalities in underground bituminous coal mine fatalities from 1995 to 2008 (Mark et al., 2011). During the same time period, smaller ground falls between roof support elements injured up to 400 miners annually (Mark et al., 2011).

Given the limitations of common empirical approaches and the inherent scaling issues associated with laboratory studies, numerical models were used to analyze the pillar-overburden relationship. The majority of numerical modeling in academia and industry is conducted using continuum methods, which require some of the same assumptions as analytical methods (namely approximation of the rockmass as a continuous body).

Coal measure (i.e. sedimentary) rock can be highly discontinuous; depending on depositional environment, tectonic history, and current mining-induced stresses, the network of bedding planes, laminations, and fracture sets violates the continuum material assumption on which most research and practice relies on. Discontinuum modeling allows for explicit separation of intact blocks and more accurately captures large-strain behavior of a discontinuous rockmass (Jing, 2003). The use of discrete fracture networks (DFNs) can mimic the distribution of joints and bedding planes found in the subsurface. In this study, the discrete element method (DEM) as implemented in Itasca's Universal Distinct Element Code (UDEC) allowed for modeling the explicit separation of horizontal bedding planes and vertical joints in overburden materials. Due to the complex nature of the research, the project begin with relatively simple studies focused on well-constrained problems that can be readily compared against in-situ observations and analytical methods documented in the literature (i.e. deformation characteristics of individual pillars/entries; immediate roof stability in individual entries; settlements associated with full panel extraction). Increasing complexity was then introduced to mimic more realistic geomining conditions (i.e. panel-scale production loads, depillaring, gob formation, and abutment loading)

Ultimately, there should be no falls of ground if existing "conservative" design methods are accounting for all relevant aspects of rockmass mechanical behavior appropriately. This is clearly not the case, and

additional complexity must be accounted for to attempt to capture a more realistic representation of local and global stability in underground coal mines.

There is a pressing need to investigate the interdependence of the pillars and overburden and to identify critical parameters that have historically been ignored in pillar design methodologies. The Alpha Foundation identified five key research questions related to this topic; these are:

- Can pillar strength be estimated from tributary area loading at collapse and are coal pillar capacities being overestimated in conventional tributary area design evaluations?
- Do coal pillars fail or yield prior to overburden failure or does the overburden failure cause pillar failure?
- Do coal pillars act to reinforce the overburden, and how?
- What effect does horizontal stress, horizontal bedding, and vertical joints play in overburden stability?
- What effect does the in-situ vertical stress have on pillar response? How does the in-situ stress effect the mining-induced compression required to produce pillar yielding and failure?

These are addressed in this study by investigating roof stability its purported self-supporting capacity, and its effect on pillar loading. Identifying how the roof and pillar interact to maintain local and global stability can be practically incorporated into analysis methods to increase their accuracy with a limited increase in complexity. These analyses are primarily based on estimations of pillar load at collapse using the tributary area theory (TAT) and an estimation of pillar strength using the Mark-Bieniawski (MB) equation, both of which are used compared to numerical model results in this study. Identifying the controls on local and global stability will allow for increased safety in underground room and pillar mines.

The following assumptions were utilized in the research presented herein.

- The study only considers two-dimensional approximations of real mining conditions; pillar load increases associated with hypothetical de-pillaring operations “out-of-plane” will be simulated through added loads at the top of the model (e.g. per Mohamed et al., 2016)
- Although fracture networks corresponding to pre-existing natural rock fractures (including bedding planes) will be represented in the models, the growth/development of new fractures cannot be explicitly modeled using the proposed approach; we assume that an inelastic continuum representation of blocks between pre-existing fractures is sufficient to allow the overall overburden mechanics to be represented
- The explicit representation of overburden fractures in panel-scale models were not extended fully to surface; continuum properties were applied to the upper portion of the overburden
- The study only considered cases where pillar deformation and strength characteristics were not controlled by discrete structural features within the pillar
- Given that the pillars are modeled as a continuum, no pillar support will be explicitly modeled (per Sinha & Walton, 2017)
- Model cases presented in this research represent a large range of behavior. Some are used as end-member cases to isolate and investigate mechanical behavior of individual system components (i.e. pillar, and overburden) relative to behaviors theorized in the literature (Frith & Reed, 2018), while others approach potentially realistic geomining conditions.

The four Specific Aims as outlined in the original project proposal are as follows:

1. Establish an approach for numerical representation of pillar strength

2. Establish an approach for numerical representation of roof and overburden mechanics
3. Develop baseline numerical models to test illustrative conceptual model cases
4. Quantify parametric interactions and influences on overburden and pillar stability

3.0 Research Approach

The following section outlines the specific aims and tasks, and their respective background, methods, and analyses implemented in accomplishing the aforementioned specific aims. Technical results are also discussed in this section, while the broader impacts regarding the goals of the research are discussed in the following sections.

Specific Aim 1 – Establish a Numerical Representation for Pillars

Task 1.1 – Parameter Determination

The numerical investigation of complete pillar-overburden systems requires that appropriate model representations for each system component are developed. The objective of this section is to select a constitutive model and corresponding input parameters that is capable of simulating coalmass behavior. Sinha and Walton (2018) recently developed a rock yield criterion, called the progressive S-shaped yield criterion, that is based on a mechanistic understanding of damage processes in brittle rocks. Given that coal behaves in a brittle manner (Mishra and Nie, 2013; Kim et al., 2018), the authors used this yield criterion to model the damage evolution in the pillar.

The progressive S-shaped criterion is built upon the precursory works of Kaiser et al. (2000), Diederichs (2003), and Kaiser and Kim (2008), and combines the Cohesion-Weakening-Frictional-Strengthening (CWFS) strength model (Martin and Chandler, 1994; Martin, 1997; Hajiabdolmajid et al., 2002) at low confinement and a shear yield model at high confinement (Hudson and Harrison, 1997). The criterion has three major thresholds: (a) Yield threshold: The low confinement portion corresponds to the Crack Initiation threshold, while the high confinement portion is an approximation of Mogi's Line; (b) Peak threshold: The low confinement portion corresponds to the Spalling Limit (Diederichs, 2007), while the high confinement portion is the Crack Damage threshold (Martin and Chandler, 1994); (c) Residual threshold: This is a degraded variant of the peak threshold and corresponds to a 30-50% reduction in friction angle (Martin and Chandler, 1994). Figure 1a shows the different components of the progressive S-shaped criterion. The yield threshold evolves to the peak threshold over a specific range of plastic shear strain values (ϵ^{ps}; proxy for damage) and then ultimately decays to the residual threshold.

To determine a set of coal mass parameters, we used the yield criterion to model the damage evolution in a longwall pillar in Australia (West Cliff mine). The particular panel under consideration is located 480 m below surface and is a part of a two-entry chain pillar system. Based on the mine geometry, a 1 m thick (pseudo plane-strain condition) FLAC^{3D} model was developed and simulation was conducted in three stages: (1) In the first stage, the model was run without any excavation until mechanical equilibrium was achieved. Pre-mining horizontal stresses of 16.3 MPa and 3.6 MPa (per Mohamed et al., 2016) and a vertical stress equivalent to the depth of mining were applied to the model. (2) The next stage consisted of developing the entry using the traction reduction method (Mohamed et al., 2016). In this method, elements inside the excavation are removed while applying forces equivalent to the pre-mining load on the boundary gridpoints. The forces are progressively relaxed until they become negligible. The second stage replicates the development loading condition in field. (3) In the final stage, the vertical stress along the top of the

model was increased by 0.2 MPa/step to simulate the retreat of the longwall face. The model was brought to equilibrium after each increment of vertical stress.

The model input parameters were constrained by matching the extensometer and stress measurements made at the site by Colwell (2006) through an iterative manual back-analysis process. Figure 2 compares the model results with the field measurements. The excellent correspondence between the model predicted displacements and stresses and those obtained through in-situ instrumentation provides confidence that the newly developed criterion can be applied to coal and coal measure rocks.

During the course of model runs in the later sections, it was found that the parameters calibrated to the coal at the West Cliff mine were too strong for general application. The reason is likely related to the fact that the parameters were developed initially for a deep coal mine (480 m) but is used here for a maximum overburden depth of 200 m. To resolve this issue, the authors re-calibrated the progressive S-shaped yield parameters to match the peak strengths predicted by the Mark-Bieniawski equation for width to height ratios (W/H) of 2, 4 and 6.

In these pillar compression models, the roof and floor were elastic, with modulus and Poisson's ratio of 8 GPa and 0.2, respectively, and a constant velocity boundary condition was applied to the model top boundary while keeping the bottom boundary fixed. Figure 1b shows the stress-strain curves obtained after calibration. The corresponding peak pillar strengths, as predicted by Mark-Bieniawski equation (pillar length set to infinity as UDEC operates in a plane-strain mode), are also shown using dotted lines. The models were able to match the peak strengths well and they also exhibited a transition from brittle to pseudo-ductile behavior with increase in W/H ratio (Esterhuizen et al., 2010).

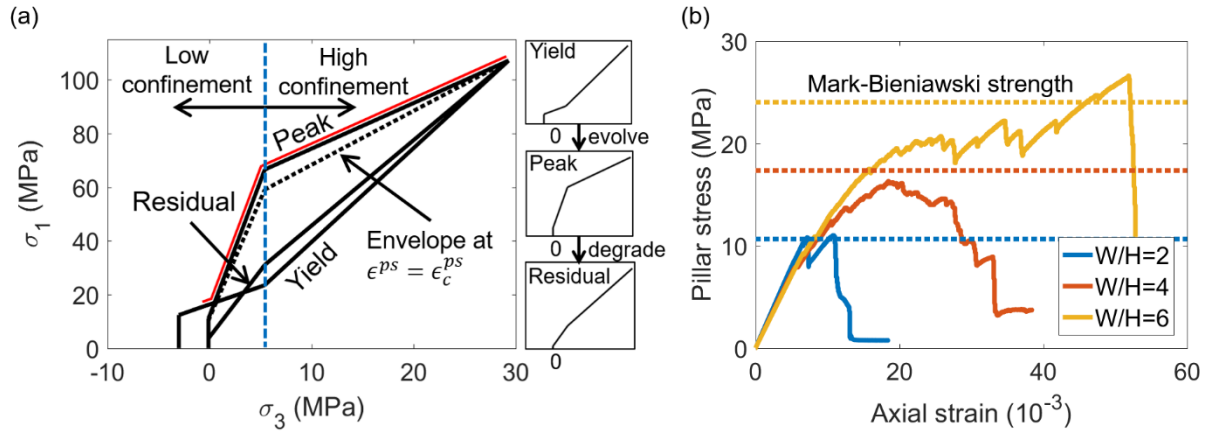

Figure 1: (a) Thresholds for progressive S-shaped yield criterion (Sinha and Walton, 2020); the red line shows the ultimate strength envelope (upper bound for all damage states) at each confining stress, which is tri-linear, or approximately "S-shaped", (b) Pillar stress-strain curves for W/H=2, 4, and 6. The dotted lines represent the corresponding strength as predicted by the Mark-Bieniawski equation.

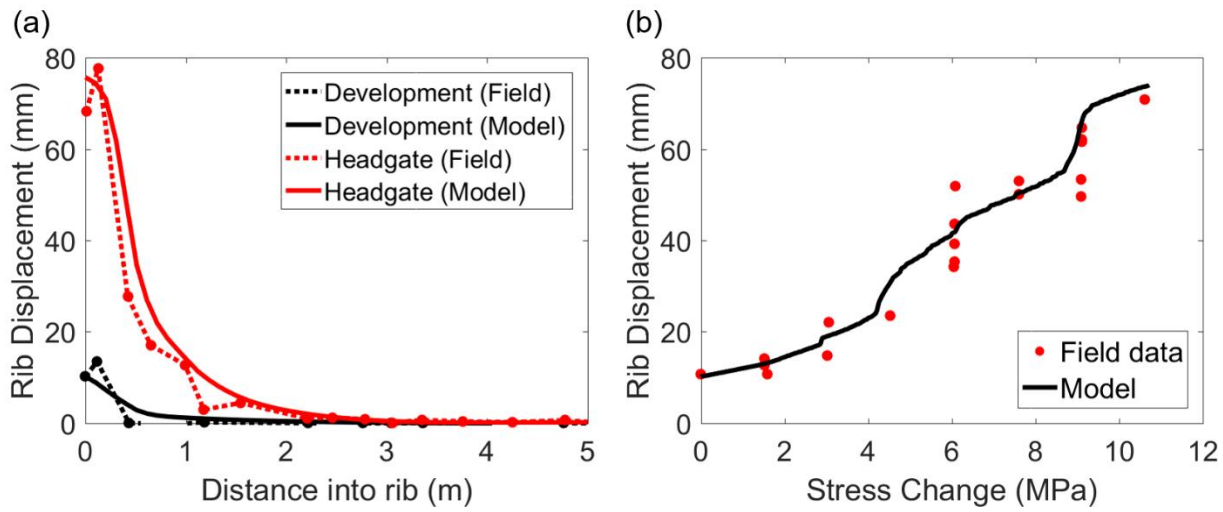

Figure 2: (a) Rib displacements from extensometer in FLAC3D model, (b) Displacements as a function of stress change from field data and the FLAC3D model (Sinha and Walton, 2020).

Since the purpose of this calibration was to obtain a representative set of coal mass parameters, no interface or joints were incorporated between the host rock and the pillar. However, as models ran in subsequent sections were focused on the interaction between the overburden and the pillar and consequently included interfaces, an analysis was performed to understand how the interfaces might affect the response of the pillars. For that purpose, the W/H=3 model was chosen and the boundary between the pillar and the host rock was simulated using a Continuously Yielding (CY) joints with initial and intrinsic friction angles of 15°. With inclusion of the joints, the peak pillar strength dropped from 14.7 MPa (corresponding Mark-Bieniawski strength is 14 MPa) to 11.6 MPa. Such a drop in strength is expected, as interfaces allow for slippage and de-confinement of the pillar (Iannacchione, 1990).

Specific Aim 2 – Establish an Approach for Numerical Representation of Roof and Overburden Mechanics

Frith & Reed (2018) recently argued that the coal industry might be wise to "focus more intently on … 'overburden stability' design parameters" than continue to rehash statistical analyses of pillar strength based on assumptions that neglect overburden behavior. Completion of Specific Aim 2 has developed 10,368 unique models and confirmed their behavior is realistic through the use of well-vetted analytical and empirical methods. These include the voussoir beam analog (Diederichs & Kaiser, 1999), Coal Mine Roof Rating (CMRR) (G. M. Molinda & Mark, 1994), and Analysis of Roof Bolt Systems (ARBS) (Mark et al., 2001). Results were analyzed using binary logistic regression to identify the most significant inputs governing roof stability to inform future portions of the study.

Task 2.1 – Develop and Validate Individual Entry Voussoir Beam Models

Prior to developing single-entry voussoir beam models, multi-jointed elastic voussoir beam models were created in UDEC based on the range of material and discontinuity properties presented in Diederichs & Kaiser (1999) as a calibration step. The presence of multiple joints, rather than a single midspan joint (i.e. traditional voussoir theory), more closely resembles roof conditions that will be modeled in future tasks. The assumptions and boundary conditions utilized in this study adhere closely to those in Diederichs & Kaiser (1999) with one exception: once voussoir arching is allowed to develop with effectively elastic joints (i.e. high cohesive strength, non-zero tensile strength), joint constitutive models were changed to continuously yielding in order to capture the effect of inelastic joints on voussoir beam mechanics. The

continuously yielding joint model has been shown to more accurately capture joint displacement under large displacements (Poeck, 2016) and is implemented in future, more complex, modeling efforts. 1 m thick, jointed voussoir beams of various length and E_{rm} were tested; initially, all intact material was modeled as elastic. General model setup and magnified block deformation of a voussoir beam at equilibrium is shown below in Figure 3.

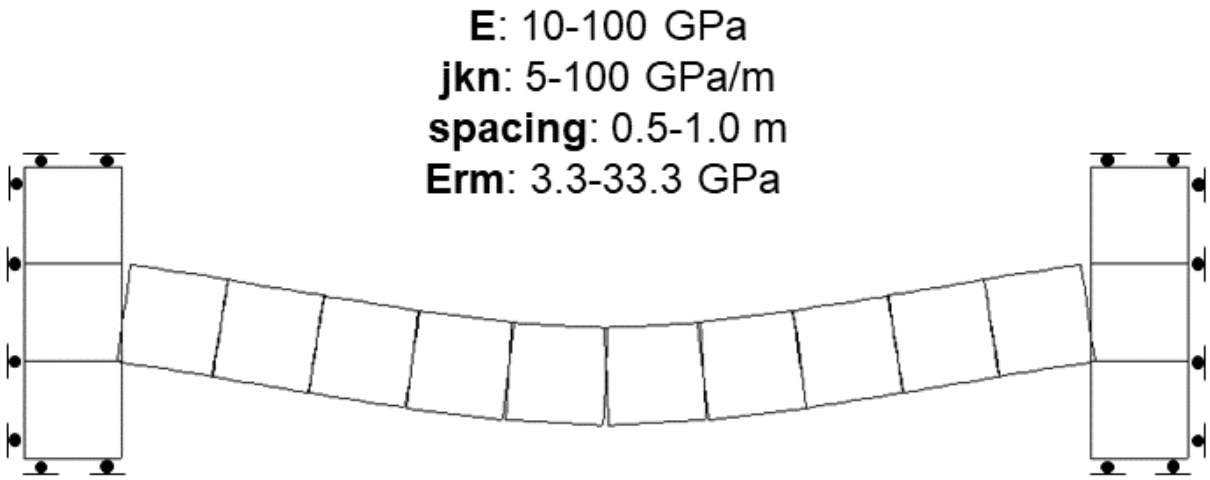

Figure 3: Simple voussoir beam model boundary conditions shown at equilibrium state with a deformation magnification. Range of parameters modeled are listed above. E – Young's Modulus, jkn – joint normal stiffness, E_{rm} – rockmass modulus.

The model solution method in Diederichs & Kaiser (1999) was replicated by running models in multiple stages; the first stage featured extremely strong joints to allow deflection to occur and horizontal stresses to develop in the voussoir beam. Subsequent stages altered the intra-span joints to realistic Mohr-Coulomb strengths and continuously-yielding joints to model the impact of more realistic discontinuities once voussoir arching has developed. Every time joint parameters were altered, the model was run to equilibrium. Initially, model results matched expected deflections; however, model results of stress magnitude deviated significantly from analytical predictions. Further investigations into material properties and model conditions were conducted on 10 m long, 3.3 GPa E_{rm} beams and found that the interaction between mesh size and block rounding had a significant effect on both deflection and stress magnitude results.

Following establishment of optimal mesh size and block rounding, the initial models were rerun, and their results confirmed UDEC's ability to capture voussoir mechanics and associated limitations. Replicating previous results provides a foundation for alteration of voussoir beam geometry in in-situ loading conditions such as a single entry.

The voussoir mechanical response was then tested in multiple single-entry models. In order to confirm that the voussoir beam analog could be applied in more realistic loading conditions and future modeling efforts, the previously tested voussoir beam geometry (i.e. 10 m span, 3.33 GPa E_{rm}) was modeled as the immediate roof and overburden in multiple single-entry models. End member cases are shown below in Figure 4.

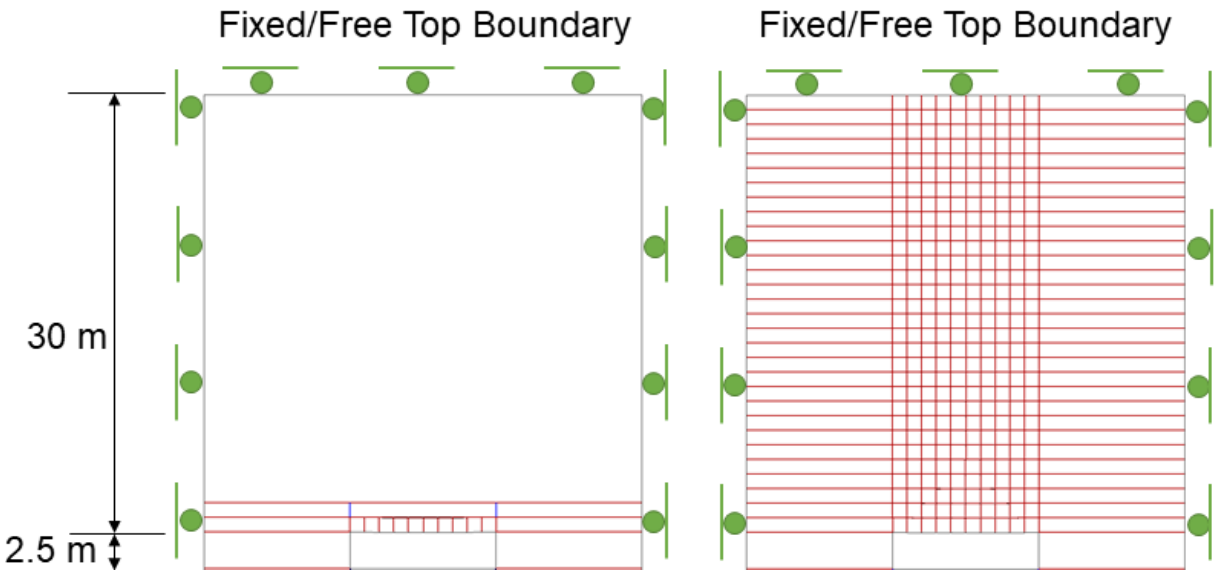

Figure 4: Example single entry voussoir models depicting boundary conditions, and model geometry. Bottom half of the model excluded for clarity.

Equivalent elastic moduli were assigned to the non-voussoir areas in the pillar and floor. Half coal pillars were modeled using elastic properties to isolate the impact of yielding pillars from the impact of explicit voussoir representation, as well as stress magnitudes and ratios in the subsurface. The models were tested at entry depths of 30 and 100 m below surface with in-situ stress ratios ranging from 0.25-2.0. Model overburden ranged from a single voussoir layer in the roof to a discrete fracture network (DFN) composed of voussoir blocks spanning the entry and extending to the top of the model. Models were analyzed in unsupported and bolted configurations.

Maximum vertical deflection and maximum midspan stress from the immediate roof layers of unsupported single-entry voussoir models are compared to analytical predictions and results from the literature in Figure 5.

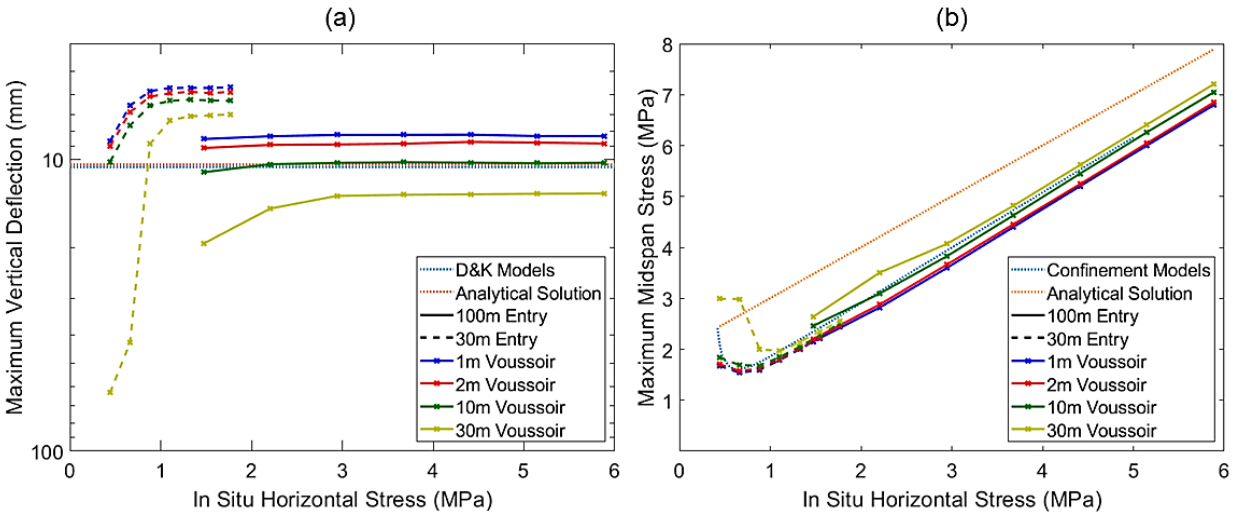

Figure 5: Unsupported single-entry voussoir model immediate roof displacement (a) and midspan horizontal stress (b) results showing the impact of in situ stresses and the increase in horizontal stress on elastic voussoir beam mechanical response.

Note that in the maximum midspan stress plot (Figure 5b) results are compared with the voussoir beam models featuring horizontal confining stresses of identical magnitudes, isolating the effect of other in-situ loading conditions (i.e, surcharge loading, abutment influence, pillar influence). Furthermore, based on the linear increase in stress observed in those models, the analytical solution from Diederichs & Kaiser (1999) was adjusted by adding the applied in-situ horizontal stress to the predicted stress, showing a clear trend. Results deviate from the modified analytical solutions by a constant margin; however, recall that voussoir analytical predictions overestimate midspan stresses and underestimate abutment stresses. Stresses shown in Figure 5b are from the midspan of the immediate roof.

These results indicate that the height of the explicit voussoir DFN and associated additional surcharge loading has a significant impact on voussoir beam mechanical behavior. Most significantly, this impact is observed at lower stress ratios in shallow entries where limited stress arching occurs in the roof, and surcharge loads incurred by the presence of contiguous voussoir beams create additional displacement via discontinuous sliding along abutment blocks. Even at higher horizontal stress where deflection of the voussoir beam is continuous (i.e. no abutment slip occurs), the minimum differences in roof displacement and maximum midspan stress are 57% and 6.1%, respectively, for varying heights of explicit voussoir in the roof. This indicates that surcharge loading can also significantly increase expected displacement and stress development of voussoir beams in high horizontal stress conditions.

The voussoir single-entry models were then run with rockbolt elements installed on 1.5 m spacing, using calibrated input parameters from Bahrani & Hadjigeorgiou (2017). Results were similar to their unsupported counterparts discussed above, except for an average decrease in stable displacement by 33% and an approximately 1 MPa decrease in midspan and abutment horizontal stress across all models tested. However, bolting did not reduce displacements for low horizontal stress cases where high surcharge loads and lack of confinement led to abutment slip failure of the immediate roof and overburden.

Bolted voussoir single-entry model results indicate that bolt parameters are behaving as expected, carrying loads in the bolts and reducing the stress magnitude in the immediate roof. The overall behavior remains true to voussoir mechanics and expected bolt behavior, where an increase in the stiffness of the system leads to a decrease in displacement and maximum expected stress. Bolted model results further confirm that in-situ roof conditions and mechanical behavior can be generally represented by the voussoir beam analog. However, if bolts do not extend into a competent layer that is supported via self-support or in-situ horizontal stresses in the roof, the roof displacements only decrease by an average of 7% from the unsupported case due to abutment slip failure (i.e. neither beam building nor suspension support is activated) Rockbolt elements decrease horizontal stresses in the midspan of the immediate roof by approximately 50%. However, the magnitude of stress at the abutment remains largely unchanged, indicating that standard vertical roof bolts may have little effect in terms of preventing crushing at the roof-pillar boundary (Figure 6).

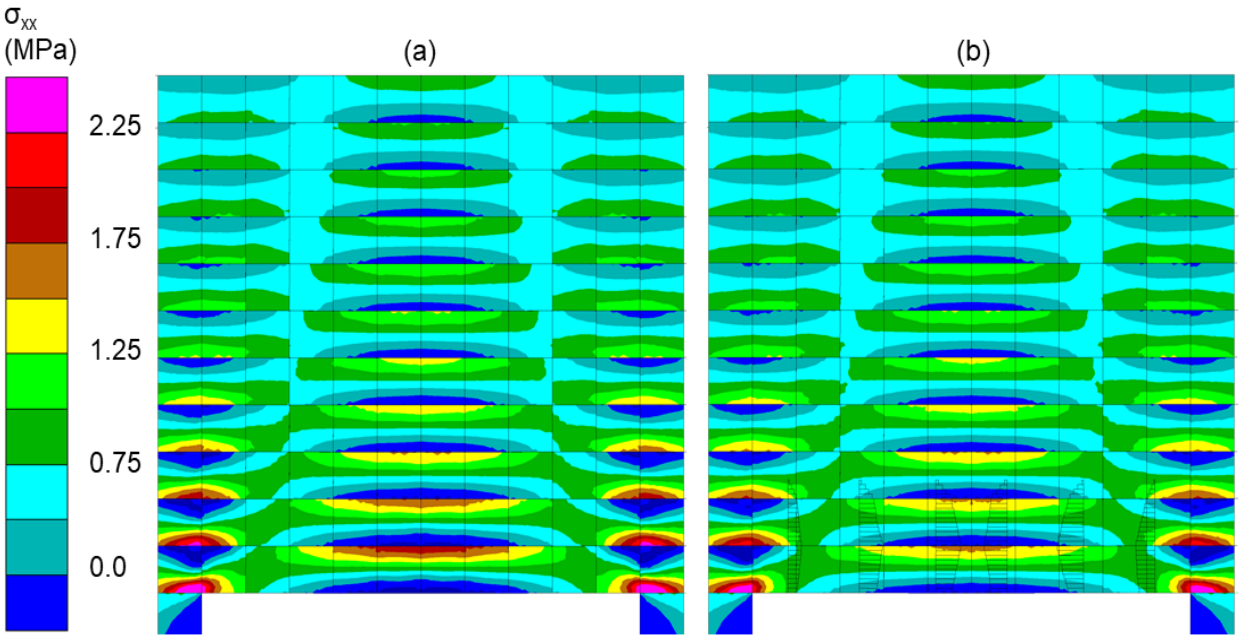

Figure 6: Comparison of horizontal stress distribution in immediate roof of unsupported (a) and bolted (b) models at 30 m depth (k_o = 1.0). The maximum load carried by the rockbolts is approximately 11.3 kN.

Systematic analysis of voussoir beam mechanical behavior under a large range of loading conditions has provided a reliable, repeatable analog for analysis of model roof stability. Parametric sensitivity analysis of baseline voussoir models has identified a key interaction between block rounding and zone size. A foundation for analyzing more complex roof behavior has been successfully developed through simple adjustments to existing analytical solutions. Accounting for applied horizontal stresses, orthogonal joints, and the presence of rock bolts is a practically applicable use of the voussoir analog in more realistic scenarios. Furthermore, the voussoir beam analog is a useful tool in the analysis of more complex numerical model results (i.e. predicting or classifying stability). Analysis of a voussoir DFN has provided a repeatable discontinuous medium that can act as a control case for the effect of changes in random joint distribution due to changes in model geometry. Completion of Task 2.1 has successfully provided an understanding of roof stability mechanics and offer a foundation by which we shall further investigate how pillars reinforce that stability in the roof and overburden. The findings of Task 2.1 validate the use of the voussoir beam analog for model analysis and identification of jointed roof stability. Voussoir beam mechanics may not be applicable to all coal-mine roofs in-situ (i.e. massive, or heavily jointed), but represent a valuable reference case for the more complex geomining conditions considered in the explicit joint models in this study.

Task 2.2 – Develop and Validate Individual Entry Rockmass Model

The previously-used single-entry model with elastic pillars was utilized to investigate more realistic roof and overburden conditions. As shown in Figure 7, the single-entry model geometry consists of two bounding half-pillars of w/h 8.0 (w/h=4.0 modeled explicitly due to symmetry conditions), 6.0 m entry span, 2.5 m entry height, and features a simplified, homogeneous overburden (i.e. no geologic heterogeneity other than the stochastic DFN).

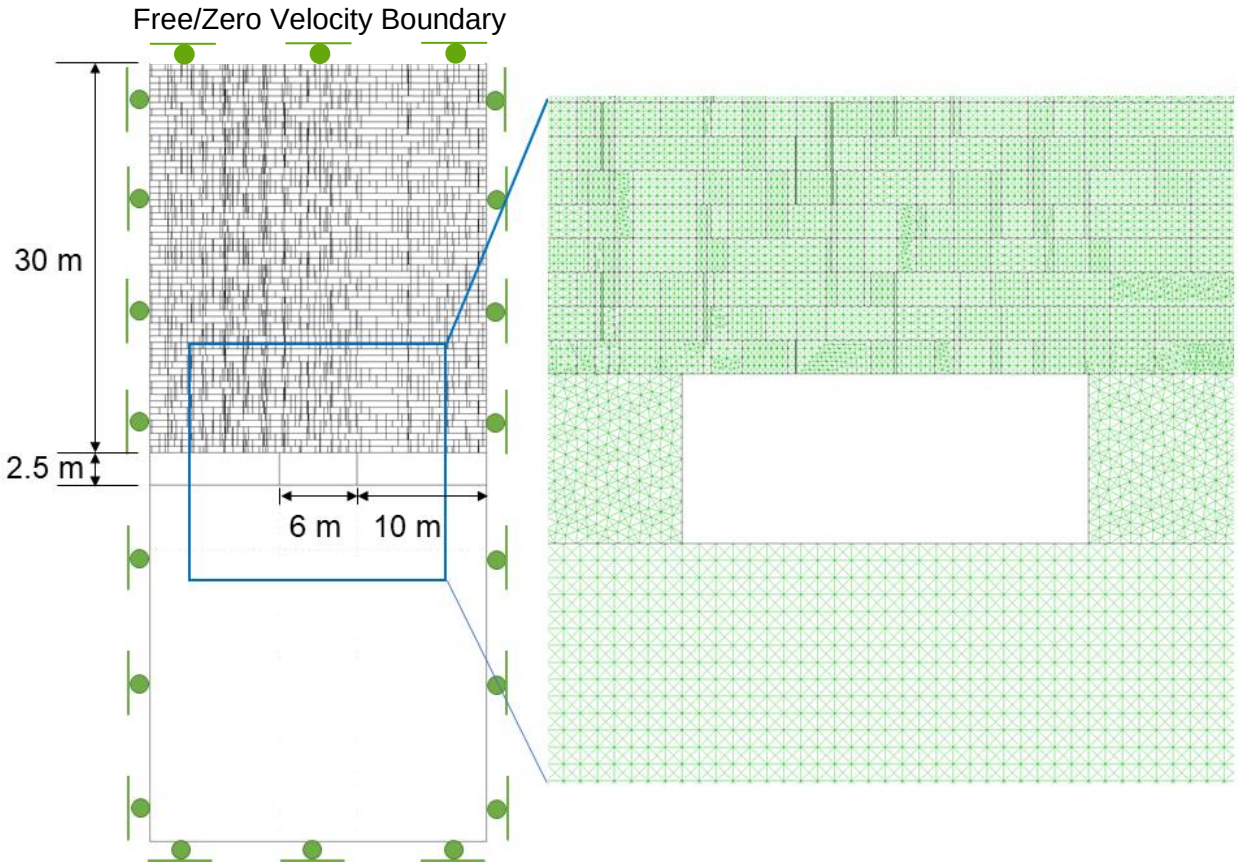

Figure 7: Example single entry model depicting boundary conditions, model geometry, mesh density, and overburden DFN.

Modeling half of each bounding pillar imposes a horizontal symmetry condition, allowing the models to focus on local roof stability. This assumes that deformation is mirrored to an infinite set of additional entries on either side of the model. The top of the model is a free surface for 30 m deep entries and a fixed velocity boundary for deeper cases. The remaining boundaries have zero velocity conditions imposed in the direction of their normal.

Contacts between the pillar and the roof were modeled with the same strength and stiffness properties as the roof DFN. The model floor was considered elastic with a stiffness calculated to approximate an equivalent continuum rockmass modulus of the fractured roof. While some coal mine roofs do not exhibit cross-jointing as pronounced as is shown in Figure 7, such geometries are necessary to allow block separation to occur in the models. This is one of the stated limitations of DEM modeling. However, jointed roofs have been documented by Molinda & Mark (2010) and are described as contributing to roof failure. Coal pillars were modeled using an inelastic constitutive model from Sinha and Walton (2018) and were initially assigned parameters that led to negligible pillar yield in the models at the depths considered to isolate roof behavior.

Model parameter combinations were selected based on existing literature (Hsiung et al., 1993, Esterhuizen et al., 2010; Bastola and Chugh, 2015) to cover a range of realistic possible behaviors. Overburden material parameters were selected to approximate the mechanical behavior of sedimentary rockmasses ranging from laminated shale to massive sandstone (Table 1).

Table 1: DEM overburden parameters analyzed in this study for parametric sensitivity analyses; note that variables in rows highlighted with the same color were varied concurrently.

Geometry					
Depth to Entry (m)	30	100	200	---	---
Span (m)	6	---	---	---	---
Pillar w/h	8	---	---	---	---
In-Situ Stress Ratio	0.5	1	2	---	---
BT (m)	0.5	1	---	---	---
Rock Material Properties (Field Scale)					
	Weak SUBI	Strong SUBI	EBP	Elastic Soft	Elastic Stiff
G (Pa)	4.17E+08	3.33E+09	1.25E+10	4.17E+08	1.25E+10
K (Pa)	5.56E+08	4.44E+09	1.67E+10	5.56E+08	1.67E+10
E (Pa)	1.0E+09	8.0E+09	3.0E+10	1.0E+09	3.0E+10
Poisson's Ratio (v)	0.2	0.2	0.2	0.2	0.2
Density (kg/m3)	2.35E+03	2.35E+03	2.35E+03	2.35E+03	2.35E+03
Cohesion (Pa)	2.50E+06	7.50E+06	1.50E+07	---	---
Tensile Strength (Pa)	5.00E+05	1.00E+06	2.00E+06	---	---
φi (◦)	25	32	39	---	---
ψ (◦)	4	8	12	---	---
Cr (Pa)	1.00E+05	1.00E+05	1.00E+05	---	---
φr (◦)	25	30	35	---	---
Tr (Pa)	0	0	0	---	---
SUBI jci (Pa)	1.00E+05	2.00E+06	---	---	---
SUBI jt (Pa)	2.00E+04	4.00E+05	---	---	---
SUBI jφi (◦)	10	20	---	---	---
SUBI jdil (◦)	0	4	---	---	---
CY Joint Material Properties					
jkn (Pa/m)	5.00E+10	---	---	---	---
jks (Pa/m)	5.00E+09	---	---	---	---
jen/jes	0/0	---	---	---	---
Initial (φi)/Intrinsic (φ) (◦)	35/30	25/20	15/15	---	---
jr (mm)	0.001	---	---	---	---
Joint Network Geometry					
Angle <sd> (◦)	90 <0>	90 <10>	---	---	---
Gap <sd> (m)	2BT <2BT>	2BT <2BT>	---	---	---
Trace <sd> (m)	4BT <2BT>	2BT <0.75BT>	---	---	---
Spacing <sd> (m)	0.25 <0.5>	1 <1.5>	---	---	---

BT=Bedding Thickness sd=standard deviation

Three zone constitutive models were used for the different material cases. The SUBI constitutive model was selected to implicitly account for closely spaced bedding planes between explicitly modeled discontinuities. Stronger, massively bedded rocks were modeled using elastic-brittle-plastic (EBP) and elastic constitutive models. The continuously yielding (CY) joint constitutive model was implemented to gradually decay joint strength from an initial (i.e. peak) to an intrinsic (i.e. residual) friction angle as a function of plastic shear displacement. Eight distinct DFNs are created based on the joint network geometry parameters, their geologic characteristics are described in

Table 2.

Table 2: DFN ID and qualitative description of vertical joints.

DFN ID	Cross Joints	Persistence	Spacing	CMRR Spacing-Persistence Rating*
1	Vertical	High	Close	20
2	Vertical	High	Wide	25
3	Vertical	Low	Wide	27
4	Vertical	Low	Close	21
5	Sub-Vertical	High	Close	20
6	Sub-Vertical	High	Wide	25
7	Sub-Vertical	Low	Wide	27
8	Sub-Vertical	Low	Close	21

* DFN-based CMRR spacing-persistence rating superseded by use of SUBI material properties

All combinations of the parameters listed above, coupled with 2 random DFN seeds resulted in 5,184 unique models. Each case was run unsupported and with a standard bolt pattern (4 per row) resulting in 10,368 unique models.

Note that two constant "seed" values were used for DFN creation, and each model had the same geometry, so joint network randomization did not influence the results between different models with the same DFN and random seed value. Furthermore, CMRR only accounts for the persistence, spacing, and condition of joints, not their orientation.

Initial model results featuring the Weak SUBI material properties listed in Table 1 were found to be too weak for use in modeling an entire homogeneous overburden after unrealistic plastic deformation was observed in the corresponding models. No amount of realistic bolting could prevent the roof from deforming in a highly plastic manner. An additional Moderate SUBI material property was developed to allow for more robust analysis within the ARBS system without implementing other support types. The Moderate SUBI material properties are listed below in Table 3.

Table 3: Moderate SUBI material properties.

Moderate SUBI Material Properties	
G (Pa)	3.33E+09
K (Pa)	4.44E+09
E (Pa)	8.0E+09
Poisson's Ratio (v)	0.2
Density (kg/m3)	2.35E+03
Cohesion (Pa)	5.00E+06
Tensile Strength (Pa)	7.50E+05
φi (◦)	30
ψ (◦)	6
Cr (Pa)	1.00E+05
φr (◦)	28
Tr (Pa)	0
SUBI jci (Pa)	7.50E+05
SUBI jt (Pa)	1.50E+05

SUBI jφi (◦)	20
SUBI jdil (◦)	2

A two-stage solution method was implemented for all unsupported model runs. Stage 1 consisted of applying an internal stress boundary equivalent to 70% in-situ stress following excavation. 70% was selected based on the longitudinal displacement profiles from Vlachopoulos & Diederichs (2009). Stage 2 removed the internal stress boundary and solved in accordance with the methods discussed above. Note that in some cases this two-stage approach may influence model stability relative to a more gradually staged relaxation process. However, this is only expected to be the case for models with borderline stability. Stage 1 model states were then utilized to mimic ground relaxation prior to bolt installation for the bolted model runs.

In order to compare UDEC models with empirical observations, a CMRR value was estimated for each model. Intact material cohesion and friction angle values were used to determine intact strength ratings, explicit joint (i.e. non-ubiquitous joints) friction angle was used to determine the cohesion-roughness rating, and DFN spacing and persistence, bed thickness, and presence of the SUBI material model were used to determine both the spacing-persistence rating and multiple discontinuity set adjustment. The groundwater sensitivity rating was not considered, as groundwater was not incorporated in the models.

Unsupported models were developed to isolate roof behavior from support influence and to identify model parameters that result in either self-supporting or unstable roof behavior. Models were organized into stable and unstable categories based on vertical displacement, velocity, and horizontal stress arch development the immediate roof. Figure 8 depicts a model case where horizontal stress arching through the previously validated voussoir beam analog was used to confirm self-stability in the immediate roof.

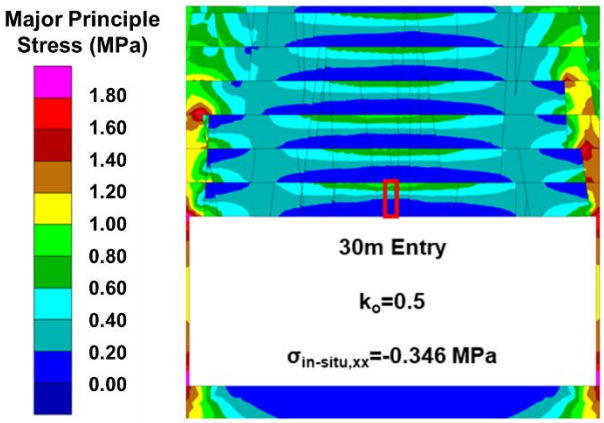

Figure 8: Development of major principal stress arching in immediate roof exceeding the in-situ horizontal stress ($\sigma_{in\text{-}situ,xx}$), indicating stable conditions; stresses were extracted from zones located in the area delineated by the red box.

Under stable conditions, as the immediate roof deflects downwards, internal horizontal stresses develop based on the voussoir beam analog described in Task 2.1 and by Diederichs and Kaiser (1999) and others. Analytical voussoir solutions predict that if the immediate roof layer in Figure 8 were a voussoir beam, it would generate approximately 0.7 MPa of horizontal compression. The in-situ horizontal stress is approximately 0.35 MPa, and the resultant maximum stress at the midspan is approximately 1.0 MPa. If the horizontal stress in the immediate roof does not exceed in-situ horizontal stress levels, this indicates that the immediate roof is not effectively transferring horizontal stress, and is therefore likely unstable. This

unstable classification is confirmed by checking maximum displacements and velocities in the roof at equilibrium. Note that manual inspection of multiple stable models at equilibrium indicated that some non-negligible velocities were present in the immediate roof. A third model solution stage was implemented to check the average velocity of the immediate roof at the target solution ratio and force the model to step forward if non-negligible velocities were still present in any of the roof zones.

Bolted models featured rockbolt elements based on models calibrated by Bahrani and Hadjigeorgiou (2017) to laboratory axial and shear load tests on fully-grouted rockbolts installed in concrete blocks. The model inputs used are listed in Table 4. Modeled bolts were 2.4 m long, 19 mm diameter, and installed on 1.2 m spacing with associated faceplates defined using UDEC's liner elements (Figure 9). As previously mentioned, bolts were installed after relaxation of the excavation boundaries to 70% in-situ stress to account for non-zero displacement prior to support installation; this approach effectively assumes that any roof deformation ahead of the excavation is elastic in nature (Walton and Diederichs, 2015).

Table 4: UDEC parameters for rockbolt and structural elements (from Bahrani & Hadjigeorgiou, 2017).

	Area (m^2)	Density (kg/m^3)	E (GPa)	Bolt YS (kN)	Bolt TFS	Plastic Moment	Shear Stiffness (N/m^2)	Normal Stiffness (N/m^2)	Shear Cohesion (N/m)	Normal Cohesion (N/m)
Bolts	$3.0x10^{-4}$	$8.05x10^3$	200.0	176.0	0.15	$2.0x10^3$	$5.0x10^7$	$1x10^{11}$	$1.2x10^6$	$8.0x10^6$
Plates	$6.0x10^{-4}$	$8.05x10^3$	200.0	---	---	---	---	---	---	---

E = Young's Modulus, YS = Yield Strength, TFS = Tensile Failure Strain

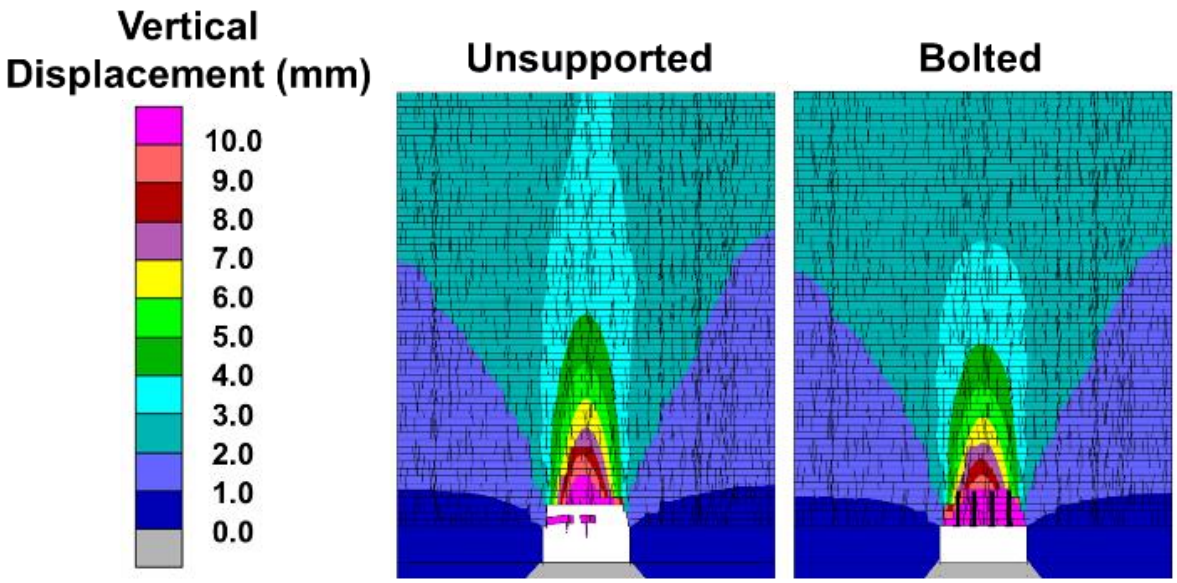

Figure 9: Example of unsupported and bolted entry model showing vertical displacement contours; 30 m entry depth, k=0.5, soft elastic material model, weak joints, sub-vertical cross-joints, 0.5 m beds, high joint persistence, and close spacing (DFN 5).

Using the model CMRR estimates along with depth to entry and intersection span, model results for unsupported entries were analyzed in relation to the ARBS discriminant (Mark et al., 2001). The ARBS discriminant is a linear relationship between the difference between actual recommended ARBS and the

difference between actual and recommended Intersection Span that was empirically determined to approximately separate stable roof cases from unstable roof cases.

Unsupported models correspond to an actual bolt intensity value of 0, and an actual Intersection Span of 6 m (19.7 ft). Suggested values were calculated based on model depth and the model CMRR estimates according to Mark et al. (2001). Although the ARBS empirical data set has no unsupported entries, assuming an ARBS of 0 for unsupported models represents an end-member case and allowed for a broader evaluation of the model behavior. Results of the comparative analysis for both DFN random seeds are presented in Figure 10. A higher negative ARBS Difference (x-axis) value indicates that a given entry is more supported (i.e. higher bolt intensity) than what the empirical discriminant is needed for stability. A negative Span Difference (y-axis) indicates that the actual span is larger than what is recommended based on empirical relationships. Cases that plot above the ARBS discriminant are predicted to be stable, and cases that plot below are predicted to be unstable.

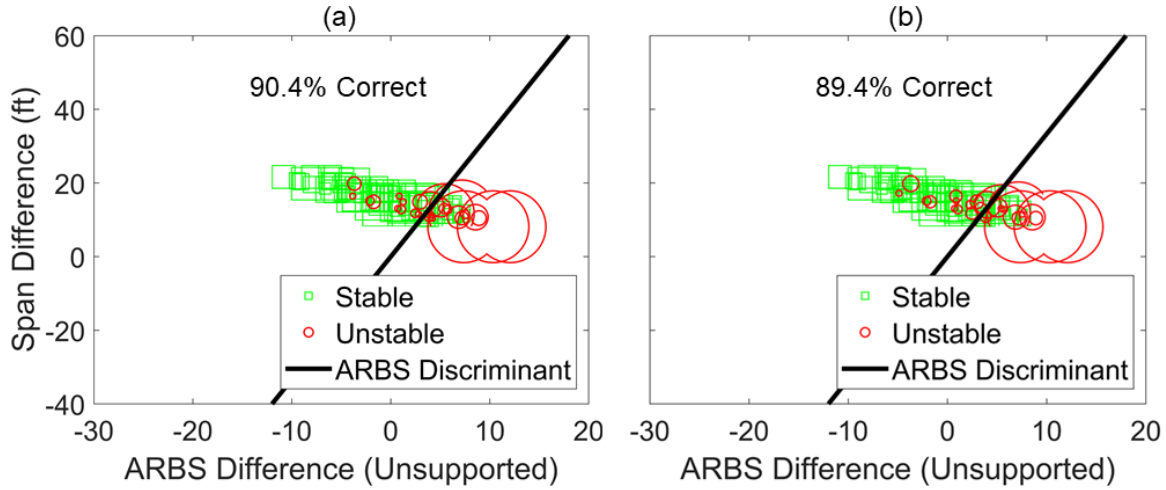

Figure 10: Results of unsupported models with random DFN seed 100 (a) and 1234 (b) and their predicted stability based on empirical formulae from Mark et al. (2001); models that plot above the ARBS discriminant are predicted to be stable by the empirical relationship; marker size indicates the number of models represented by a single data point.

The results indicate that empirical calculations and predictions based on model inputs accurately captured the relationship between CMRR, ARBS, entry depth, and intersection span with 90.4% correct classification for random seed 100 and 89.4% for random seed 1234. This also indicates that the random distribution of joints in the immediate roof is not a critical control on roof stability for the DFN cases tested (i.e. where there is no distinct major discontinuity/fault that dominates roof behavior). Although a direct comparison between empirical and numerical results is not possible, the results are consistent with the empirically derived ARBS discriminant and indicate that the models are behaving realistically (Mark et al. 2001).

Based on bolt parameters and installation geometry utilized in the bolted models, an ARBS value of 16.08 for the model support system was calculated from equation 5 given by Mark et al. (2001). Based on the relationships defined by Mark et al. (2001), it was predicted that all bolted models would be stable (see Figure 11).

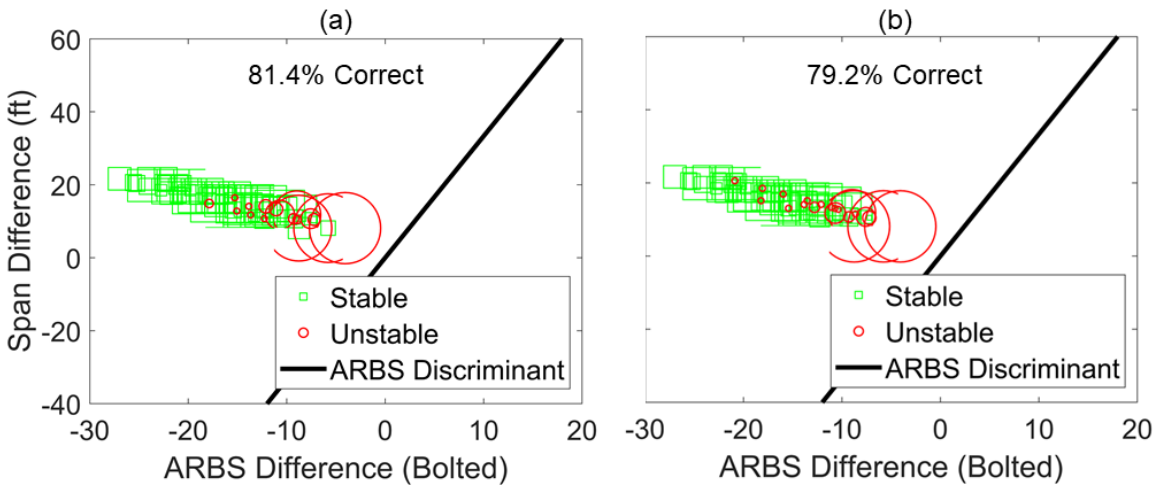

Figure 11: Results of bolted models with DFN random seed 100 (a) and 1234 (b) and their predicted stability based on empirical formulae from Mark et al. (2001); models that plot above the ARBS discriminant are predicted to be stable; marker size indicates the number of models represented by a single data point.

However, results showed 81.4% correct classification for random seed 100 and 79.2% for random seed 1234. Weak SUBI models are included in the bolted analysis, but it was found that excessive bolting with an ARBS rating of 32.16 (i.e. 8 bolts) could not stabilize "best-case" weak SUBI models. Mark et al. (2001) noted that some of the case studies which make up the ARBS empirical data had extremely weak roofs that could not be supported by only roof bolts. These cases are outside of the empirical range that ARBS is valid. Again, this relates to the inability of bolt systems to stabilize roof cases with extremely weak "intact" material (Mark et al., 2001) in both the real world and in the models.

Following confirmation of realistic behavior using established empirical methods, statistically significant model inputs governing roof stability were identified using a Binary Logistic Regression (BLR). BLR is used to identify the impact categorical input variables (e.g. material type, DFN ID Number) have on a binary output (i.e. stable, unstable roof). BLR cannot account for "perfect delineators", such as the Weak SUBI material type, where every model featuring Weak SUBI material properties was unstable. BLR fits a multi-dimensional surface of predicted stability probability between 0 and 1 that provides a predicted stability based on a given set of selected inputs. Two such slices of this multi-dimensional surface are plotted in Figure 12 below to illustrate the findings of the statistical analysis.

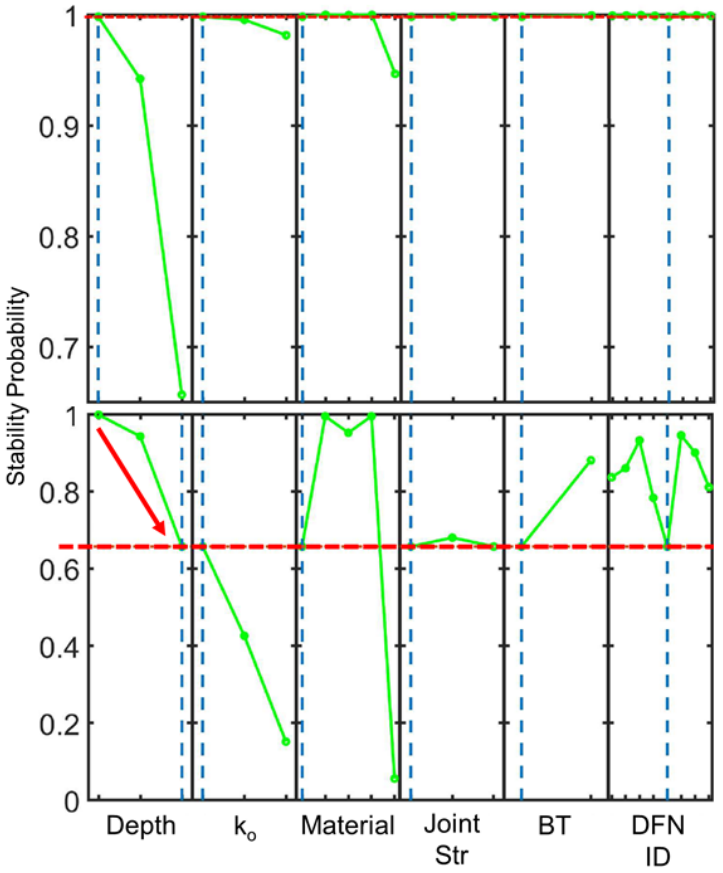

Input	Values
Depth	***30 m*** 100 m 200 m
Stress Ratio	***0.5*** 1.0 2.0
Material	***Strong SUBI*** EBP Soft Elastic Stiff Elastic Mod SUBI
Joint Strength	***Weak*** Moderate Strong
Bedding Thickness	***0.5 m*** 1.0 m
DFN ID	1,2,3,4,***5***,6,7,8

Figure 12: Two slice plots showing predicted stability of a given model condition based on selected input variables (blue vertical dashed lines). The possible inputs for each categorical variable, from left to right, are provided in the associated table (right); the baseline values for the top slice plot are bold in the table. Note that the increase in depth from 30 m (top) to 200 m (bottom) increases the number of variables (i.e. k_o, Material, Joint Strength, Bedding Thickness, and DFN ID) that are statistically significant in controlling probability of roof stability. Furthermore, note the change in range of stability probability between the 30 m and 200 m cases.

The results of the BLR indicated that at shallow entries, the probability of a stable roof condition, regardless of the other inputs, does not drop below 0.95. As entry depth increases, the range of predicted stability in unsupported roofs varies from 1 (stable) to 0.15 (likely unstable). This is reflected in the empirical suggested ARBS value, $ARBS_G$, which is based on entry depth and CMRR. Recall that CMRR is reflected in the categorical input variables Material, Joint Strength, Bedding Thickness, and DFN ID. Note that while k_o is not explicitly accounted for by Mark et al. (2001), a relationship between entry depth and horizontal stress exists where observations were taken.

The results of the parametric sensitivity analysis presented in this study confirm that some cases of bedded and jointed sedimentary roofs do have self-supporting capacity as modeled herein. This self-supporting capacity is most-influenced by entry depth; in low-stress conditions, most unsupported roofs will remain stable. However, as depth increases, fine-scale bedding (as represented using the SUBI constitutive model in this study), and to a lesser extent, intact material properties such as stiffness and strength, in-situ stress ratio, explicit DFN type, and bedding thickness had increasing impact on roof stability. Surprisingly, explicit joint strength had very little impact on roof stability. Stable bolted models provided similar results,

indicating that support mechanics are strongly related to roof self-supporting capacity, but decrease the impact that increasing depth has on roof stability. This is not the case in extremely weak roofs, as discussed previously.

The completion of Task 2.2 identified the most significant inputs governing roof stability in single-entries and confirmed that the range of geomining conditions modeled were behaving realistically. Results were verified as realistic via comparison to empirical observations of roof stability and statistical analysis of parametric sensitivity results identified the key interaction between model inputs and roof stability. A subset of parameters tested in Task 2.2 were identified as significant controls on roof stability and were selected to represent a range of roof conditions to examine the impact of pillar deformation on roof and overburden stability as discussed with respect to Task 2.3.

Task 2.3 – Test Pillar Deformation Influence on Overburden Stability

Through binary logistic regression, the combination of model inputs that most significantly impacted the probability of roof stability were identified. 27 models (

Table 5) from DFN random seed 100 that covered the range and combination of most significant inputs were selected and run with the previously calibrated coal pillar model from Specific Aim 1.

Table 5: DFN seed 100 models selected for analysis with calibrated coal pillars.

Model ID	Depth	Stress Ratio	Material Type	Joint Strength	BT	DFN ID
161	30 m	0.5	Strong SUBI	Weak	0.5 m	1
353	30 m	0.5	Stiff Elastic	Weak	0.5 m	1
449	30 m	0.5	Soft Elastic	Weak	0.5 m	1
4577	30 m	2.0	Mod SUBI	Weak	0.5 m	1
4578	30 m	2.0	Mod SUBI	Weak	1.0 m	1
4585	30 m	2.0	Mod SUBI	Weak	0.5 m	5
3041	200 m	0.5	Strong SUBI	Weak	0.5 m	1
3042	200 m	0.5	Strong SUBI	Weak	1.0 m	1
3049	200 m	0.5	Strong SUBI	Weak	0.5 m	5
3050	200 m	0.5	Strong SUBI	Weak	1.0 m	5
3233	200 m	0.5	Stiff Elastic	Weak	0.5 m	1
3329	200 m	0.5	Soft Elastic	Weak	0.5 m	1
3337	200 m	0.5	Soft Elastic	Weak	0.5 m	5
4001	200 m	2	Strong SUBI	Weak	0.5 m	1
4002	200 m	2	Strong SUBI	Weak	1.0 m	1
4009	200 m	2	Strong SUBI	Weak	0.5 m	5
4010	200 m	2	Strong SUBI	Weak	1.0 m	5
4289	200 m	2	Soft Elastic	Weak	0.5 m	1
4297	200 m	2	Soft Elastic	Weak	0.5 m	5
4961	200 m	0.5	Mod SUBI	Weak	0.5 m	1
4962	200 m	0.5	Mod SUBI	Weak	1.0 m	1
4969	200 m	0.5	Mod SUBI	Weak	0.5 m	5
4970	200 m	0.5	Mod SUBI	Weak	1.0 m	5
5153	200 m	2	Mod SUBI	Weak	0.5 m	1
5154	200 m	2	Mod SUBI	Weak	1.0 m	1
5161	200 m	2	Mod SUBI	Weak	0.5 m	5
5162	200 m	2	Mod SUBI	Weak	1.0 m	5

18 variations of each model selected from Task 2.2 were run featuring every combination of the properties listed below in Table 6, as well as in both unsupported and bolted configurations.

Table 6: Pillar parameters and model geometries tested in Task 2.3 for each Task 2.2 model case.

Depth to Entry (m)	Baseline	300	450
Pillar W/H	8	4	---
Pillar Stiffness (E)	3.00E+09	1.50E+09	4.50E+09

This resulted in 972 additional models investigating the interaction between roof and pillar at the single-entry (i.e. local) scale. Maximum model depths were increased from 200 m to 450 m by increasing the applied stress boundary condition in order to push pillars to post-peak behavior. The models were run using the same zone size, boundary conditions, and solution methods as their Task 2.2 counterparts. However, the average pillar stresses and strains, roof displacement, and material yield in the roof and pillars were collected every 100 steps and extracted as history files. This allowed more thorough analysis of pillar-overburden interaction as yield propagated throughout the entry.

Coal parameters were calibrated in Specific Aim 1 to match the predicted MB strength in a simplified loading condition. However, the only models that approached their MB strength were W/H=4 pillars in

450 m entries. The effect of overburden properties on TAT loading and MB strength is investigated further in Specific Aim 4. The influence of significant roof stability inputs (i.e,, realistic loading conditions) were considered in Task 2.3 to address the goals of this task, mainly, the *interaction between system components that could lead to catastrophic mine failure as observed in the cases of the Crandall Canyon and Coalbrook mine disasters.*

To address the question of how pillars affect roof stability and how roof properties affect pillar loading, we must first answer the question of "which yields first?". Note that yield and failure are not synonymous terms, yield can occur without functional failure of a given element.

Functional failure of the entry can occur due to failure of the roof, failure of the pillars, or total system failure. Obviously, this depends heavily on the state of stress and the contrast in material properties between the roof and the pillar; a weaker roof is more likely to induce yield in the roof, whereas a stronger roof will induce yield in the pillar. This is reflected in the model results that track roof and pillar yield. Figure 13 below highlights this observed phenomenon in two of the calibrated pillar models featuring different roof material properties.

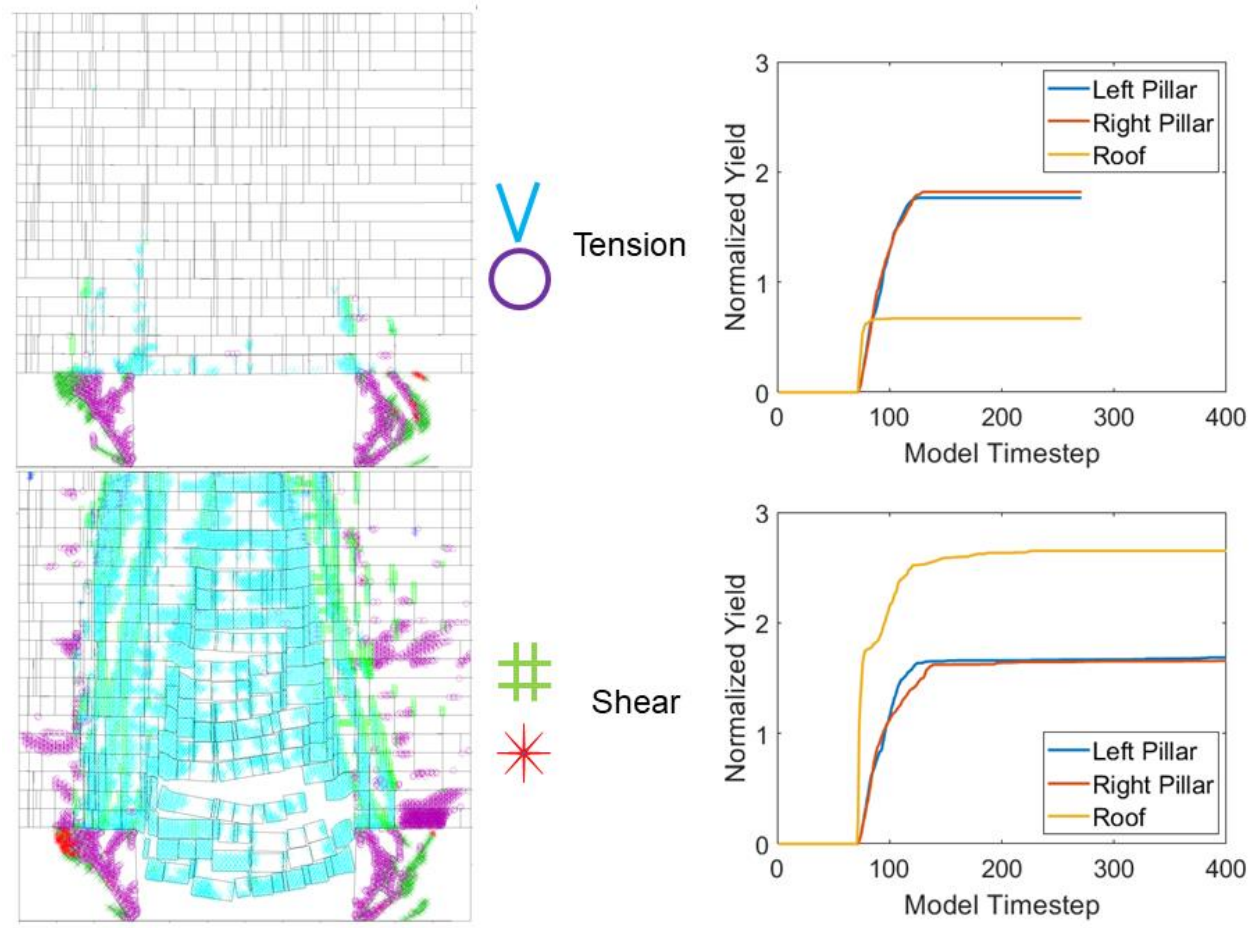

Figure 13: Model image (left) depicting yielded zone element distribution and generalized roof stability for Model ID 3041 - Strong SUBI (top) and Model ID 4961 - Moderate SUBI (bottom) material types in identical loading conditions (entry depth=300 m, DFN 1) and pillar properties (W/H=8, E=1.5 GPa). Model extractions (right) comparing normalized yield of roof and pillar elements. Normalized Yield is calculated as the number of yielded elements divided by the mesh element density (i.e. mesh elements per unit area) in a given system component (i.e. immediate roof beam or pillar).

Normalizing the number of yielded elements to the given mesh element density in each system component allows a direct comparison to be made regarding the development of yield. For example, in the Moderate SUBI case depicted in Figure 13, 874 zones have yielded in the immediate roof beam between the two pillars and 856 elements have yielded in the left pillar. If those two values are compared, it would appear that the degree of yield would be almost equal. Dividing that value by the mesh density shows a much clearer trend, as depicted in Figure 13. In Figure 13 the pillars have incurred some yield, but are still functional. Looking at deeper entries that incurred total pillar failure, *yield* can initiate in either the pillars or the roof, but total entry (i.e. global) *failure* consistently initiates in the pillars, even in the weakest roof cases. However, this does not mean that if the pillars were to remain stable, the roof will follow suit. These results are consistent with the findings of Frith & Reed (2018).

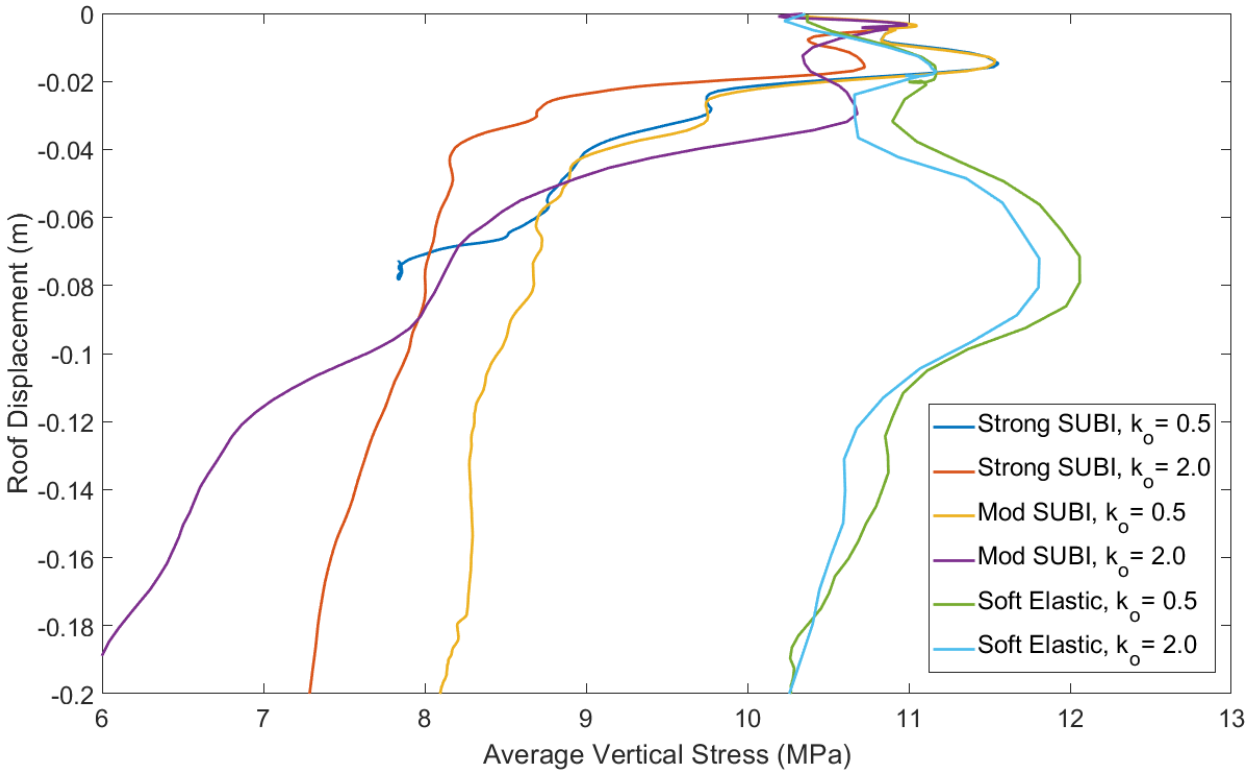

Figure 14: Plot comparing roof displacement and average vertical stress in the left pillar for models featuring the same DFN but various material types and horizontal stress ratios (see

Table 5).

Figure 14 shows a comparison of roof displacement and pillar loading for various roof types and in-situ stress ratios at an entry depth of 450 m and DFN 1 (vertical joints). Note that roofs in inelastic models with high horizontal stress ratios deflected approximately 3 mm prior to pillars attaining their peak strength. Inelastic roof models with low horizontal stress ratios deflected approximately 14 mm prior to peak pillar load. These roof displacements are not indicative of a massive roof failure, indicating that the pillars fail first when complete collapse occurs, independent of inelastic roof properties. However, this does not indicate that the roof has no impact on how the pillar fails. Elastic roof models behaved very similarly to the inelastic, high stress ratio models discussed previously. They deflected approximately 20 mm prior to preliminary shedding of load, followed by changes in roof displacement and pillar loading to a peak pillar load at 80 mm of roof displacement. Interestingly, unloading and reloading of the pillar occurred in all roof and stress conditions. Secondary loading of the pillar exceeded the previous peak load in elastic roofs and low horizontal stress ratios, further reinforcing the previous findings that less roof yield means additional pillar loading and yield.

The evidence suggests that although *yield* can initiate in either the roof or the pillars, global mine *failure* initiates in the pillars. Furthermore, the progressive failure is governed by strength contrast and horizontal stress conditions in-situ. Following initial pillar failure, roof failure is more likely to exceed or match the failure of the pillars in high horizontal stress conditions.

Interestingly, the presence of sub-vertical joints and changes in bedding thickness did not significantly impact the load transfer between inelastic roofs and pillars in the pre-peak and peak loading. However, changes in DFN and Bedding Thickness impacted the equilibrium average stress state of the pillar at high horizontal stresses. Pillar loading of both entry pillars in DFN 1 (vertical cross joints) models were loaded almost identically, but the presence of sub-vertical cross joints impacted where stresses were transferred to in total entry failure. The left pillar tended to take on more load and incur less yield than the right pillar in these cases. Furthermore, in low horizontal stress ratio, elastic roof models featuring different DFNs had a remarkable effect on load transfer in the post peak.

The completion of Task 2.3 provided valuable insight on the load transfer relationship between overburden and pillars at single-entry scales. Pillar failure was identified as the critical system component governing global stability in an infinite entry array. Parameters that impact stress transfer through the roof (i.e. DFN, horizontal stress, stiffness, and strength) significantly alter the peak and post-peak loading of the pillars. These impacts are further investigated at the panel (i.e. global) in Specific Aim 4.

Task 2.4 – Develop and Validate Panel Model

Representing explicit fracture networks throughout the entire overburden at the panel scale is not practical due to the high computational demand. Furthermore, for the purposes of this study, our primary concern is the interaction between pillar and overburden. The influence that discrete fractures may have on pillar loading likely decays with increasing distance from the pillar-roof boundary. An 8.0 m height of explicit DFN was chosen based on caving heights of approximately 3 times seam thickness as noted by (Majdi et al., 2012). Explicit bedding thicknesses of 0.5 m and 1.0 m were examined for their accuracy and overall effect on model run-time. The remainder of the overburden was represented using a weak, homogenous strain-softening ubiquitous joint model (SUBI), with “Black Shale” parameters from Tulu et al. (2016). Panel geometries (width of panel to height of overburden) were developed in accordance with previous empirical observations of surface subsidence from Australian longwall coal mining (Ditton & Frith 2003).

Three panel geometries capturing sub-critical, critical, and super-critical panel widths were modeled. Model results of surface subsidence were extracted and compared to the empirical observations in Ditton & Frith (2003). The coal seam was modeled as elastic to isolate the potential impacts of roof and overburden properties on subsidence. Implicit and explicit gob model results in comparison to the empirical dataset is presented below in Figure 15.

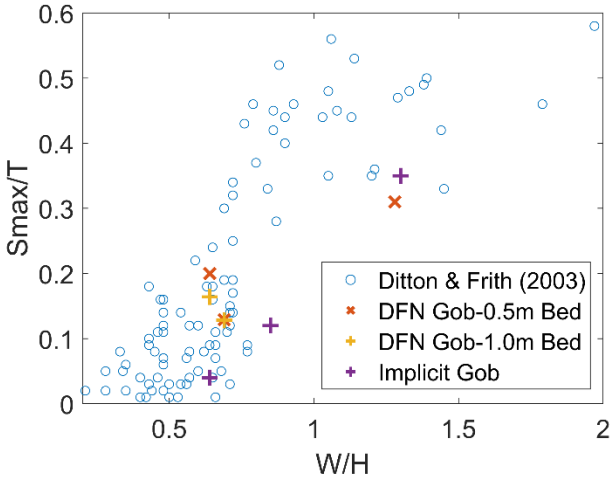

Figure 15: Empirical confirmation of homogenous SUBI overburden representation (UDEC) and implicit gob (FLAC) models.

Larger panel W/H cases tended to slightly underestimate subsidence, which is attributed to the difficulty in modeling large amounts of gob compaction in an explicit DFN without using material parameters that would lead to block overlap issues causing model termination. Therefore, as a point of comparison, the originally proposed scope was expanded to include an alternative gob representation. Specifically, the gob model used by Tulu et al. (2016), which updates the gob modulus per Salamon's hardening curve (Salamon, 1990), was tested and was found to provide similar subsidence estimates to the discrete gob models at lower W/H values and slightly higher subsidence estimates at larger W/H values (consistent with the data presented by Ditton & Frith (2003)). Based on the results of Task 2.4, select panel-scale models in Specific Aim 4 were also analyzed using the continuum implicit gob models (Figure 16). This will allow for comparison of sensitivities in the two different cases as well as deviations from TAT and MB values in future sections where the calibrated coal model is introduced to the panel-scale models.

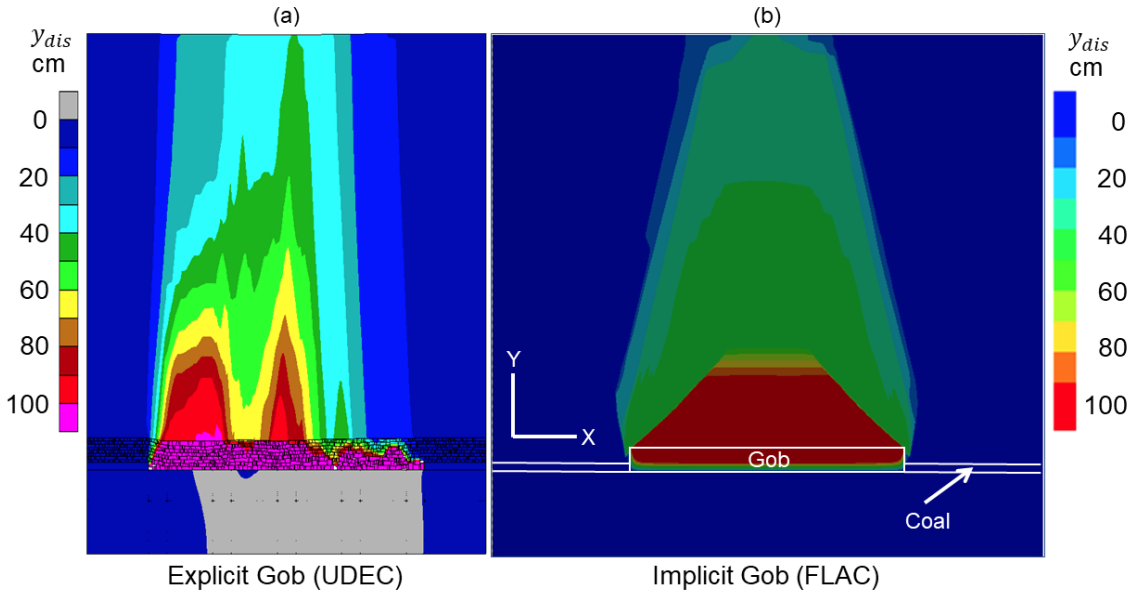

Figure 16: Vertical displacement contour plots of panel-scale models with different gob representations matching expected displacement from Ditton & Frith (2003).

Specific Aim 3 – Develop Baseline Models to Test Illustrative Conceptual Model Cases

Conceptual models are critical towards developing a sound understanding of a physical process (Starfield & Cundall, 1988). Before delving into complex panel scale models, it is beneficial to study the important mechanisms and modes of deformation in pillars and the overburden using simplified models. In this section some hypothetical cases, that are primarily based on the thought experiments of Frith and Reed (2018), are tested using simple UDEC models. While interpreting the results under this Specific Aim (especially Task 3.1), it is important to keep in mind that many of the overburden representations tested represent extreme, and in some cases unrealistic, conditions; such conditions were considered here to test the thought experiments of Frith and Reed (2018).

Task 3.1 – Develop and Test Model with Massive Rigid and Massive Elastic Overburden

Four different model classes were developed for this analysis, with the coal pillar parameters calibrated as part of Specific Aim 1:

1. Massive Rigid (modulus set to 500 GPa) overburden with vertical joints
2. Massive Rigid (modulus set to 500 GPa) overburden without vertical joints
3. Massive Elastic overburden with vertical joints
4. Massive Elastic overburden without vertical joints

In the context of overburden, the term “massive” refers to a single thick unit that contains no defects (e.g. bedding, joints, etc.) up to the surface; an example would be a thick conglomerate roof over a coal seam (Frith and Reed, 2018). The overall model setup, including dimensions and boundary conditions, is shown in Figure 17. First, the pre-mining stresses were applied and the model was brought to mechanical equilibrium, followed the development of the left entry and finally the development of the right entry. The built-in zonk-function was used for developing the entries that incrementally reduces the unbalanced boundary forces in 10 discrete stages. The vertical joints along the edge of the coal barrier as well as the joints between the coal seam and the host rock were represented using the CY model. All possible

combinations using two values each for the excavation width (6 and 10 m), mining depth (30 and 200 m), k_o-ratio (0.5 and 2), joint strength (initial/intrinsic: 15º/15º and 25º/20º), and W/H of the isolated pillar (2 and 4) were tested. Some illustrative results are shown in Figure 18.

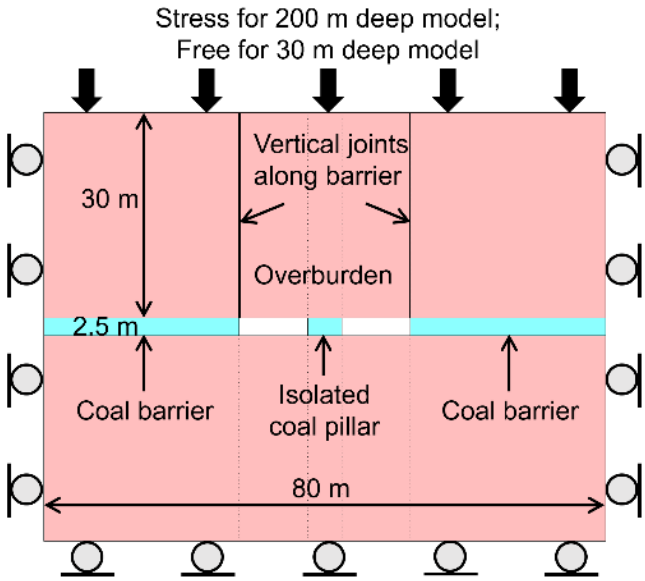

Figure 17: Model geometry and boundary conditions for Task 3.1.

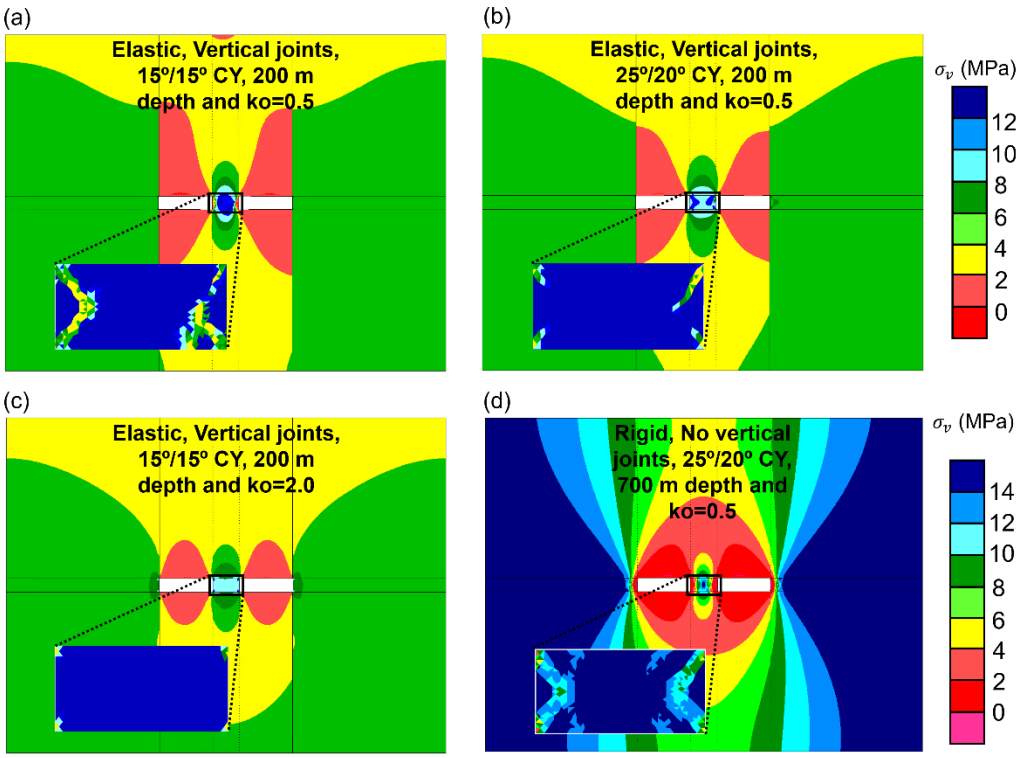

Figure 18: Vertical stress contours for four model cases. The inset shows a plot of damaged elements within the isolated coal pillar. For the model with no vertical joints, the CY parameters correspond to the joints between the coal seam and the host rock.

Frith and Reed (2018) discussed how the presence of vertical joints along the edge of the panel impacts the post-mining ground control conditions. While a vertical fracture from the coal seam all the way to the ground surface is not realistic, the models serve as a simplified analog for a fractured overburden, and thus provide insight into the failure mechanics and ground control issues that one might expect under such a geological condition. There are two factors that can affect the stress redistribution process in such a scenario: 1) Strength properties (cohesion and friction angle) of the vertical joints: If these are high, then the stresses can be transferred to the barriers; and 2) In-situ stress ratio: Higher stress ratio will allow generation of more frictional forces along the joints and allow for a smoother transfer of stresses.

Figure 18(a-c) illustrates the relative impact of these two factors on the stress redistribution process. Figure 18a is the worst case condition that has a low k_o-ratio and low joint strength parameters. As can be seen, there is an abrupt stress discontinuity along the vertical joints - since stresses cannot efficiently transfer to the barriers across a slipping joint, more load is channeled to the isolated pillar, resulting in extensive rib damage (see inset in Figure 18a). Note the relatively undamaged wall mass partitioned by the failing zones in the inset; this region was termed as 'baggage' by Kaiser et al. (1995). Figure 18b and c highlight the stabilizing effect of joint friction angle and k_o-ratio, respectively. It seems that for this set of parameters, k_o-ratio has more effect in preventing the slippage of joints, and accordingly had less yielded elements within the pillar. None of the shallower depth models posed any problem, likely due to the lower vertical stresses in these models.

In the rigid jointed models at the baseline depth of 200 m (corresponding figures are not shown), irrespective of the k_o-ratio and the joint properties, there was a sharp stress discontinuity along the vertical joints, such that only stresses corresponding to the block bounded by these vertical joints were channeled through the coal pillar. For their unjointed counterparts, the deflection of the roof was minimal due to its high flexural rigidity, and consequently the stresses were significantly lower in the coal pillar (~40-50% less than in corresponding deformable roof models). This difference arose since the modulus of the overburden was modified between a rigid and an elastic model, but the modulus of the coal seam was not. Naturally, the strains and the associated stresses in the isolated pillar were dependent on the extent to which it is was compressed by the roof.

In addition to the parameter combinations listed above, a rigid overburden model was run for a mining depth of 700 m. The respective vertical stress contour and damage state in the pillar is shown in Figure 18d. This model was run to verify the statement of Frith and Reed (2018) that a small coal pillar with factor of safety < 1 will not contribute to the overburden stability under a massive roof. Indeed, as the isolated pillar rib was damaged, a de-stressed zone was created that arched over both the entries. The pillar at this point has somewhat softened and is only carrying a small portion of the overburden load. The excess stress is transferred to the stiffer barrier pillars. The concept is similar to that used in design of yield pillars where the pillars undergo damage in a controlled manner, thereby transferring the majority of the load to the larger barrier pillars.

Task 3.2 – Develop and Test Model with Laterally Jointed Overburden

For this task, two different stratigraphies corresponding to a soft and a stiff immediate roof were chosen from Esterhuizen and Barczak (2006). A schematic of the lithologies is shown in Figure 19. A transversely

isotropic elastic model in UDEC requires five input parameters: Modulus in plane of isotropy ($E = E_1 = E_2$), Modulus in plane perpendicular to the plane of isotropy (E_3), Elastic shear modulus ($G' = G_{13} = G_{23}$), Poisson's ratio 1 (ν_{12}): characterizes lateral contraction in the plane of isotropy when tension is applied in this plane, and, Poisson's ratio 2 ($\nu' = \nu_{13} = \nu_{23}$): characterizes lateral contraction in the plane of isotropy when tension is applied in the direction normal to it. To determine each set of input parameters, the following steps were followed: a) Poisson's ratio 1 was considered to be same as Poisson's ratio 2 and these values were chosen from Esterhuizen and Barczak (2006). b) The ratio of E_3/E_1 was selected to be 1.72 (Alejano et al., 1999). E_3 for each layer was selected from Esterhuizen and Barczak (2006). c) The cross shear modulus G' ($G_{13} = G_{23}$) was calculated using the equation (Lekhnitskii, 1981):

$$G_{13} = \frac{E_1 E_3}{E_1(1 + 2\vartheta_{13}) + E_3}$$

Table 7 lists the input parameters for the different layers. The same parameter combinations, as those tested in Task 3.1, were considered in the model setup.

Table 7: Transversely isotropic elastic properties for the different rock layers.

Lithology	E_3 (GPa)	ν'	ν_{12}	$E_1 = E_2$ (GPa)	G' (GPa)
Black Shale	6	0.25	0.25	3.48	1.86
Shale	8	0.25	0.25	4.65	2.40
Sandstone	12	0.25	0.25	6.97	3.72
Limestone	20	0.25	0.25	11.62	6.21

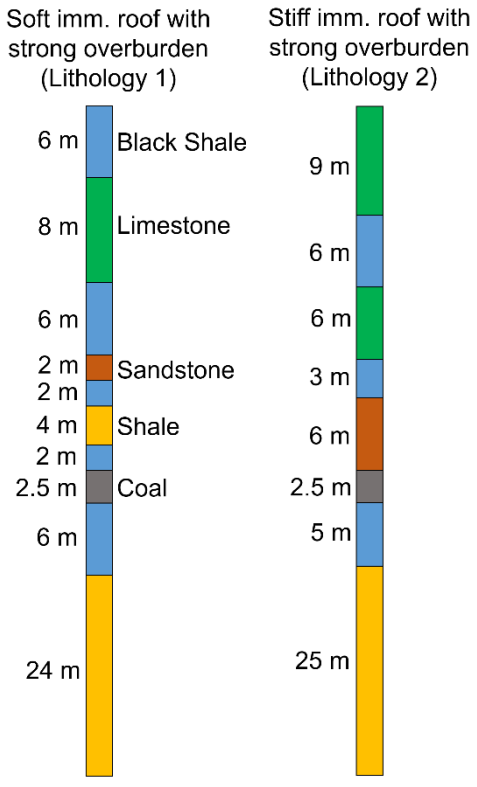

Figure 19: Schematic of the stratigraphies considered in Task 3.2 (from Esterhuizen and Barczak, 2006).

The findings from the jointed case (i.e. vertical joints at the edge of the entries) are similar to those obtained under Task 3.1 and are therefore not discussed further here. Figure 20 (a, b) shows the vertical stress contours corresponding to the W/H=2, 10 m entry width, 15º/15º joint friction angle, 200 m depth, and k_o-ratio of 0.5 case for Lithology 1 and 2, respectively. Note that Lithology 1 had a combination of black shale and shale immediately above the coal seam while Lithology 2 had a 6 m sandstone unit (see Figure 19).

A drastic difference can be noted in Figure 20 (a, b) in terms of the state of the coal pillar under equilibrium conditions. For Lithology 1, the pillar has yielded completely and has minimal load carrying capacity. In contrast, only the edges of the isolated pillar have yielded for Lithology 2. It seems that the presence of a stiff sandstone unit in the immediate roof resists the flexure of the bed as the pillar softens by surficial spalling. The vertical stress contour from a massive (elastic, not rigid) unjointed overburden model, ran as a part of Task 3.1, is also shown in Figure 20c. Based on a comparison of Figure 20 a-c, it can be inferred that overburden massiveness indeed controls the proportion of stress transferred to the barriers and the isolated pillar. A secondary conclusion is that under a soft immediate roof, a wider yield pillar might be necessary (Figure 20d; W/H=4).

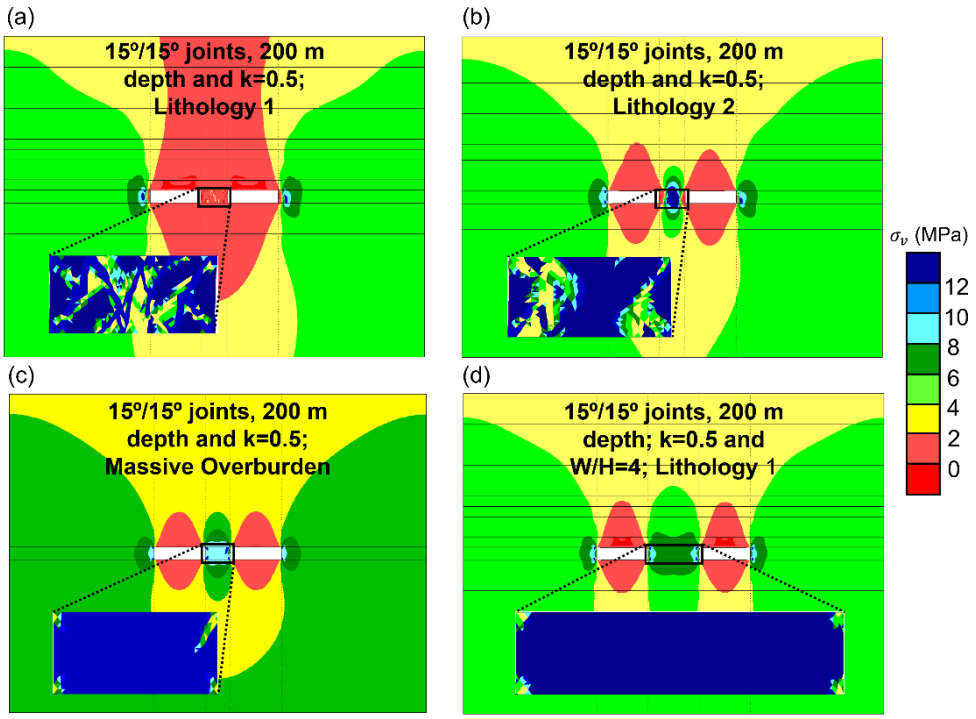

Figure 20: Vertical stress contours for four model cases. The inset shows a plot of damaged elements within the isolated coal pillar. For the model with no vertical joints, the CY parameters correspond to the joints between the coal seam and the host rock.

Some other observations made from the models ran as a part of this task are as follows:

- The average stress in the isolated pillar was consistently higher in models with stronger interface properties at the top/bottom of the pillar. This is expected as stronger interface properties result in greater frictional force mobilization along the pillar edges, which in turn "locks in" the pillar confining stress.

- Wider entries resulted in greater average stress in the isolated pillar, as the width of the pressure arch increased.
- Greater k_o-ratio resulted in greater average pillar stress only when the entries were wider (10 m); a reverse trend was observed when the entries were narrow (6 m). Greater k_o-ratio implies greater horizontal stresses in the rock layers. A likely reason for this behavior could be the limited ability to buckle into the entry when the entry size is smaller but greater ability when the entry is wider (flexural stiffness of a beam is inversely proportional to L^3).
- Wider pillars consistently had lower stresses than their narrower counterparts due to lower extraction ratio.
- For jointed models, irrespective of the lithology, the isolated pillar was fully yielded (average stress of only ~0.8 MPa at "equilibrium") at 200 m depth with ko=0.5, 10 m entry span and weaker joint properties. Increasing the k_o-ratio had the most significant effect and the isolated pillars stabilized (average stress of 8.77 MPa and 8.91 MPa for Lithology 1 and 2, respectively). Making the joint properties stronger while keeping the k_o-ratio at 0.5 had a positive effect as well, but the pillars were subjected to a somewhat greater degree of damage.
- Increasing the W/H for the cases with vertical abutment joints stabilized the isolated pillar, as squatter pillars have greater peak strength and ability to strain-harden prior to reaching the peak strength (Figure 1b).

Specific Aim 4 – Quantify Parametric Interactions and Influences on Overburden and Pillar Stability

Following development of pillar and overburden behavior (Specific Aims 1 & 2, respectively) and testing of simple conceptual models (Specific Aim 3), a panel-scale study was performed with added complexities such as multiple openings, inelastic roof layers, and various joint networks in the immediate roof.

Task 4.1 – Perform Initial Sensitivity Analyses

The baseline model was selected based on the previously completed tasks and the proposed research objectives. The baseline model featured five entries that were 6 m wide and 2.5 m high. 8 m of explicit voussoir DFN were modeled above the coal seam to control for potential impacts that changes in model geometry can have on DFN creation. Some implicit gob models were also considered for comparative analysis.

A direct sensitivity analysis was conducted on the parameters listed in Table 8 below for their individual impact on the baseline model. Non-voussoir DFNs featuring non-uniformly spaced vertical and sub-vertical joints were analyzed with two random seeds to analyze if specific joint placement has a significant impact on pillar loading.

Models were run in a similar manner as those presented in Task 2.3. Model entries were excavated following in-situ stress initialization, a 70% in-situ stress condition was applied to the excavation boundaries, and the model was run to equilibrium. Bolts and faceplates were modeled as they were in Specific Aim 2, using the rockbolt and beam structural elements, and models were run to equilibrium. Two final steps were implemented to model in and out of plane depillaring operations. To mimic in-plane depillaring, pillars were deleted and the models were run to equilibrium until the full panel was extracted, or until the model returned a "contact overlap" error. To mimic out-of-plane depillaring, a uniform stress boundary was applied to the top of the model in increments determined by the panel width, until the model could no longer step due to contact overlap. Previous modeling experience, visual confirmation, and

subsequent analysis of model results indicated that this contact overlap condition was indicative of either a local entry failure or global mine failure.

Table 8: Proposed DEM overburden parameters to be analyzed in this study for panel-scale sensitivity analyses; note that variables in rows highlighted with the same color are to be varied concurrently. The first column indicates the baseline model condition. Proposed lithologies and locations of strong beds are depicted below in Figure 22.

Geometry/Pillars/Loading						
Depth to Entry (m)	150	300	450	---	---	---
Span (m)	6	---	---	---	---	---
Production Pillar w/h	3	1	6	---	---	---
Barrier Pillar w/h	16	---	---	---	---	---
In-Situ Stress Ratio	1	0.5	2	---	---	---
No. of Entries	5	7	---	---	---	---
Strong Bed (Location)	DFN Base	DFN Mid	DFN Top	OB Base	OB Mid 4m	OB Mid 8m
Strong Bed Thickness (m)	2	---	---	---	---	---
Hetero Models	Lithology 1	Lithology 2	---	---	---	---
Pillar Stiffness	3.00E+09	1.50E+09	4.50E+09	---	---	---
Excavation Loading	1	---	---	---	---	---
Rock Material Properties (Field Scale - SUBI)						
	DFN Mod Shale	DFN Weak (BS)	DFN Strong (SS)	OB Weak (BS)	OB Strong (LS)	---
G (Pa)	3.33E+09	4.17E+08	3.33E+09	3.33E+09	1.07E+10	---
K (Pa)	4.44E+09	5.56E+08	4.44E+09	4.44E+09	1.79E+10	---
E (Pa)	8.00E+09	1.00E+09	8.00E+09	8.00E+09	2.69E+10	---
Cohesion (Pa)	5.00E+06	2.50E+06	7.50E+06	2.03E+06	1.30E+07	---
Tensile Strength (Pa)	7.50E+05	5.00E+05	1.00E+06	5.80E+05	5.80E+06	---
φi (◦)	22	20	32	20	42	---
ψ (◦)	6	4	8	2	10	---
Cr (Pa)	1.00E+05	1.00E+05	1.00E+05	2.03E+05	1.30E+06	---
φr (◦)	20	20	30	20	42	---
Tr (Pa)	0	0	0	5.80E+04	5.80E+05	---
SUBI jci (Pa)	7.50E+05	1.00E+05	7.50E+05	2.0E+05	7.55E+06	---
SUBI jt (Pa)	1.50E+05	2.00E+04	1.50E+05	3.0E+04	5.80E+05	---
SUBI jφi (◦)	20	10	20	5	30	---
SUBI jdil (◦)	2	0	2	1	6	---
CY Joint Material Properties						
jkn (Pa/m)	5.00E+11	5.00E+10	---	---	---	---
jks (Pa/m)	5.00E+10	5.00E+09	---	---	---	---
jen/jes	0/0	0/0	---	---	---	---
Initial (φi)/Intrinsic (φ) (◦)	25/20	35/30	15/15	---	---	---
jr (mm)	0.001	---	---	---	---	---
Joint Network Geometry (2 Seeds Each for Non-Voussoir DFNs)						
Angle <sd> (◦)	90 <0>	90 <10>	90 <0>	---	---	---
Gap <sd> (m)	0 <0>	1 <0.25>	1 <0.25>	---	---	---
Trace <sd> (m)	1.0 <0>	2.64 <1>	2.64 <1>	---	---	---
Spacing <sd> (m)	0.5 <0>	0.3 <0.1>	0.3 <0.1>	---	---	---
DFN height (m)	8.0	---	---	---	---	---

BT=Bedding Thickness, BS=Black Shale, SS=Sandstone, LS=Limestone, OB=Overburden, sd=standard deviation

Figure 21 shows the locations of individual strong layers in the panel-scale models. Note that strong layers (e.g., sandstone, limestone) in the DFN were modelled with higher strength and exhibit strain-softening behavior post-peak. Strong layers in the overburden are represented with weaker parameters than those in the DFN, and the post-peak behavior is modelled as perfectly plastic. This is because the presence of explicit fractures and bedding requires a stronger intact material to replicate a realistic observed behavior.

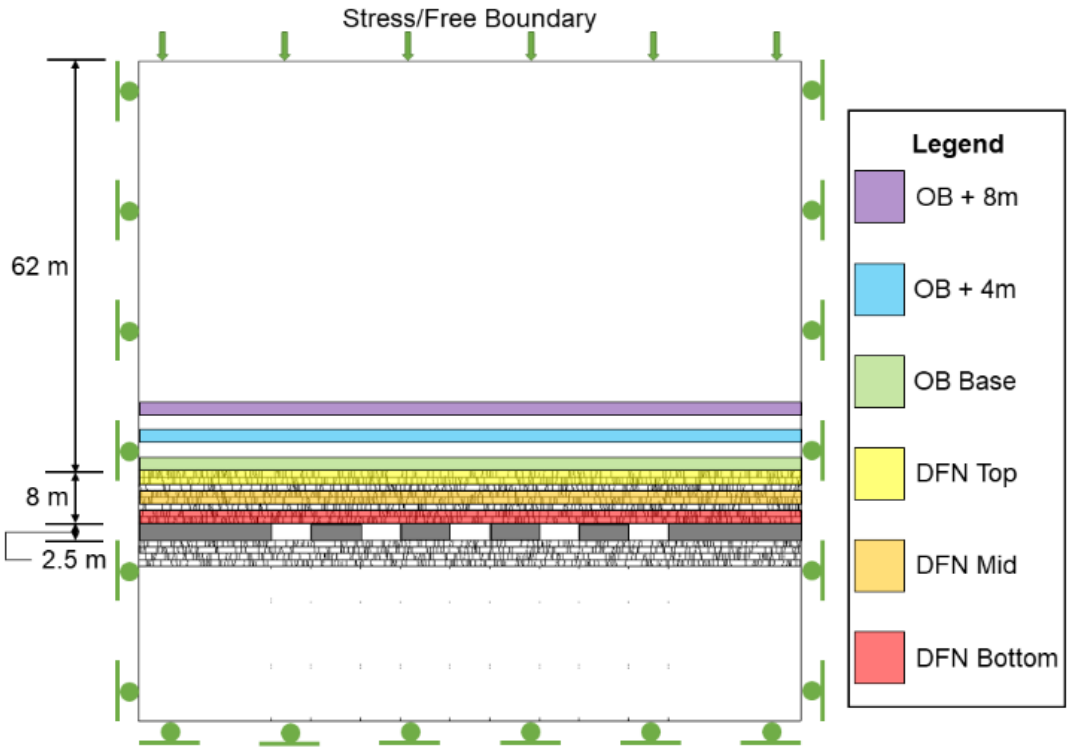

Figure 21: Figure showing the proposed location and thickness of strong layers in both the explicit DFN and the massive SUBI overburden to analyze the model response to stronger roof and overburden lithologies. Legend indicates where the strong bed will be located in relation to the continuum SUBI overburden, or the explicit DFN. OB = Overburden.

Model setup showing boundary conditions and geometry of proposed heterogeneous lithologies are shown in Figure 22. These include weak immediate roof and weak overburden (top), as well as strong immediate roof and strong overburden. Note that the areas with explicit an DFN have slightly different properties to allow for more complete representation of bulking (lithologies based on Esterhuizen & Barczak, 2006).

The model outputs such as average pillar strength (i.e, stress-strain curves), pillar stress paths, pillar factor of safety, yielded elements in the roof, floor, and pillar, and entry convergence were extracted from every model for analysis.

Model results were compared to existing analytical and empirical methods of determining pillar loading (TAT) and peak strength (Mark-Bieniawski). TAT loading was calculated by assuming overburden deadloads are evenly distributed to an infinite array of pillars, where the pre-mining stresses are simply multiplied by the extraction ratio of mined coal to unmined coal within the panel. Mark-Bieniawki pillar strength was calculated using the formula:

$$\sigma_s = 6.2 * [0.64 + 0.54\frac{W}{H}]$$

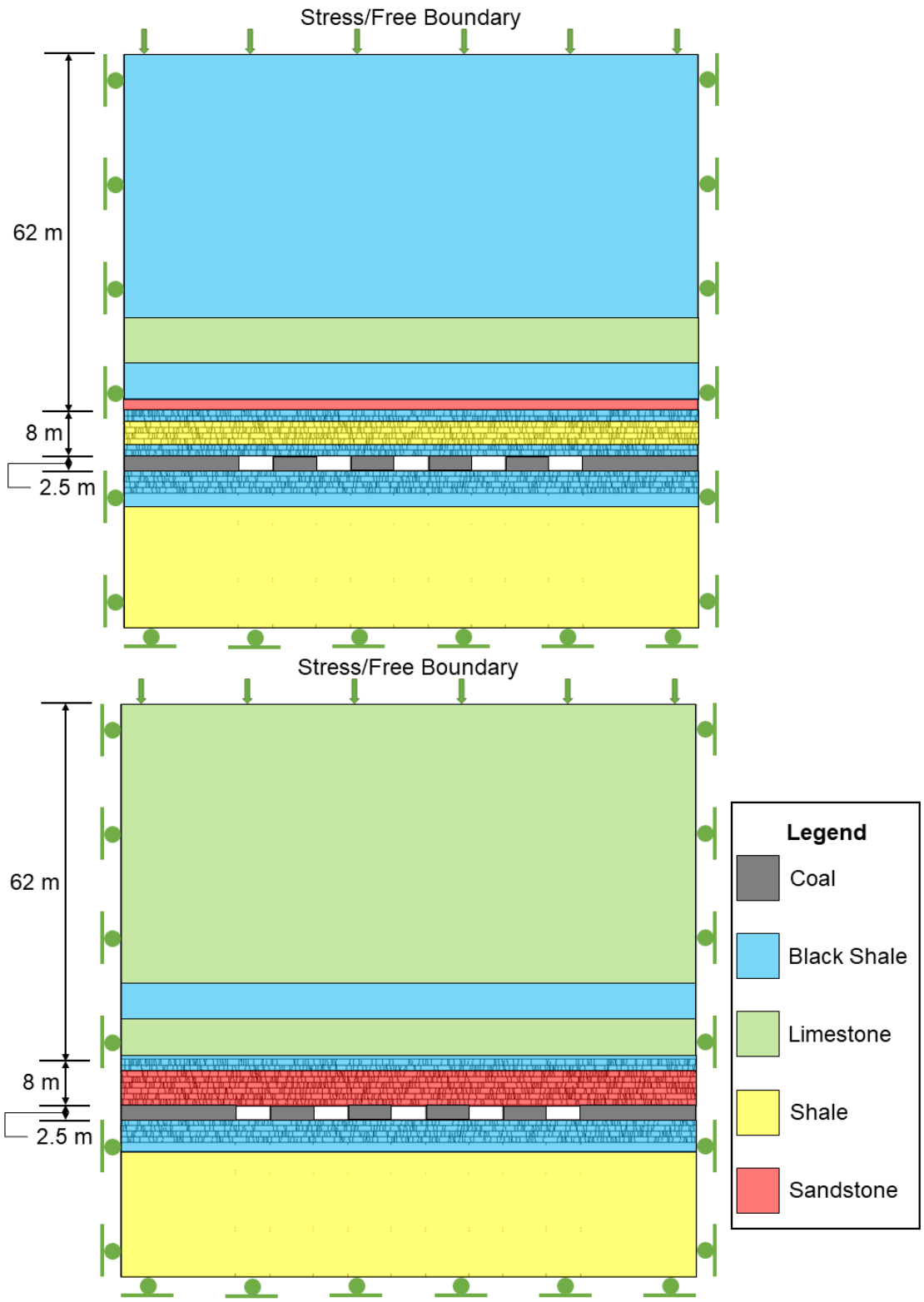

Figure 22: Figure depicting the two proposed heterogeneous stratigraphy models to tested for their impact on global stability, stress distribution, and pillar FS. Note that material properties for each lithologic unit are shown in Table 8.

Initial analysis investigated the change in average production pillar stress in relation to TAT predicted loads for the range of overburden and geometric parameters tested. In order to ensure a robust comparison, the peak load from the left-most pillar was extracted from all in-plane depillaring models to ensure that only production loads were considered; the left-most pillar was always extracted first if production loads did not incur local or global failure of the model. All of the deeper cases (300 m, 450 m), as well as the weak roof cases resulted in global pillar failure or local roof failure. However, they are included in the TAT comparison because the pillar loads extracted are production loads and they highlight the inaccuracy of TAT for given loading conditions. Out of plane depillaring was not considered in the following analysis. Figure 23 below shows the range of variation in the percentage change between predicted TAT stresses and peak pillar stresses extracted from the model cases discussed above. TAT error (%) was calculated as follows:

$$TAT\ Error\ (\%) = \frac{TAT - \sigma_{yy,average}}{\sigma_{yy,average}} * 100$$

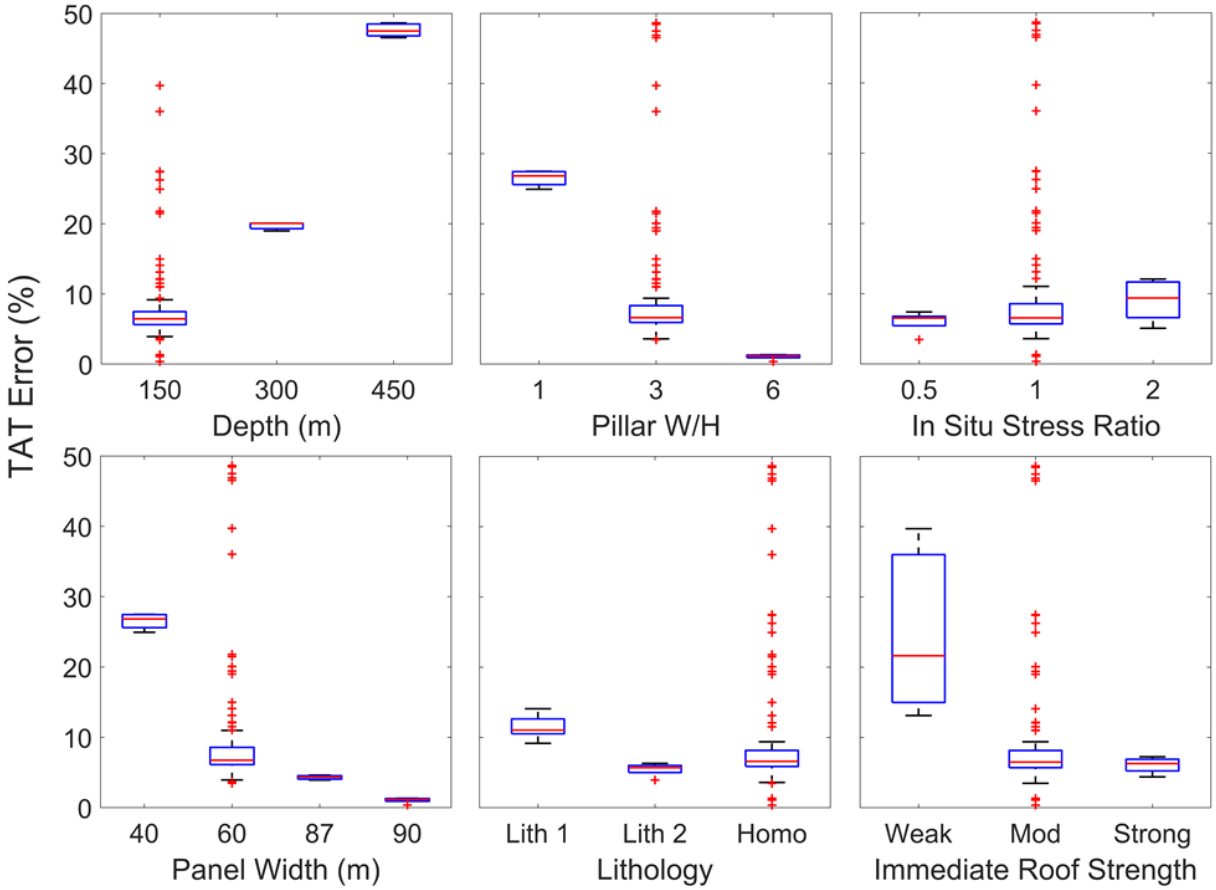

Figure 23: Comparison of the impact of significant panel-scale model inputs on TAT predicted loads. Pillar peak average stresses were compared as a percent change from the TAT predicted loads.

As expected, TAT increasingly over-predicted production pillar stresses with increasing entry depth, in-situ stress ratio, and decreasing strength, while TAT over-prediction decreased with increasing pillar W/H and panel width. Weaker hetereogeneous stratigraphy also increased TAT error, while a stronger and stiffer lithology slightly decreased TAT error. Interestingly, the intact material and explicit joint strength of the

immediate roof had little impact on TAT error. This indicates that the overall stiffness of the roof is more important that the strength of the material when determining pillar *loading*, as the Moderate and Strong roof cases had identical intact material stiffness. The results of models with strong layers in the DFN and continuous SUBI overburden, as well as those that tested changes in pillar stiffness, showed no significant change in production pillar loads and were excluded from the figure above.

A similar analysis comparing model results to the predicted MB pillar strength was conducted on all panel models with entry depths of 300 m and 450 m, as well as out of plane depillaring models, where production pillars were loaded to peak strength. Results indicated that MB pillar strength equation overpredicted pillar strength under the applied loading conditions for 300m entries by 35%, 450 m entries by 11%, and out of plane loading models by 12-24%. Explicit DFN geometry and random seed had a negligible impact on MB error when compared to other input parameters. 300 m and 450 m models were unstable prior to production loads being attained, and this made it impossible to determine which inputs were affecting TAT and MB in the same model (i.e. peak strength was not attained at 150 m and production loading was unstable in 300 and 450 m models). Therefore, an additional subset of out of plane depillaring models, which were stable under production loads and approached instability through applied stresses at the top of the model, were run with variables that corresponded to the highest levels of TAT error to determine if they had similar effects on MB pillar strength. The results of this analysis are shown in Figure 24. Note that the models featuring Weak SUBI material in the explicit DFN were the only case where every entry failed (i.e. global failure) without associated pillar yield. However, this case is considered unrealistic, since a uniformly weak overburden extending well above the entries is highly unlikely; additionally, in reality, such a weak roof would likely be properly supported with cable bolts and steel straps, which are outside the scope of this study.

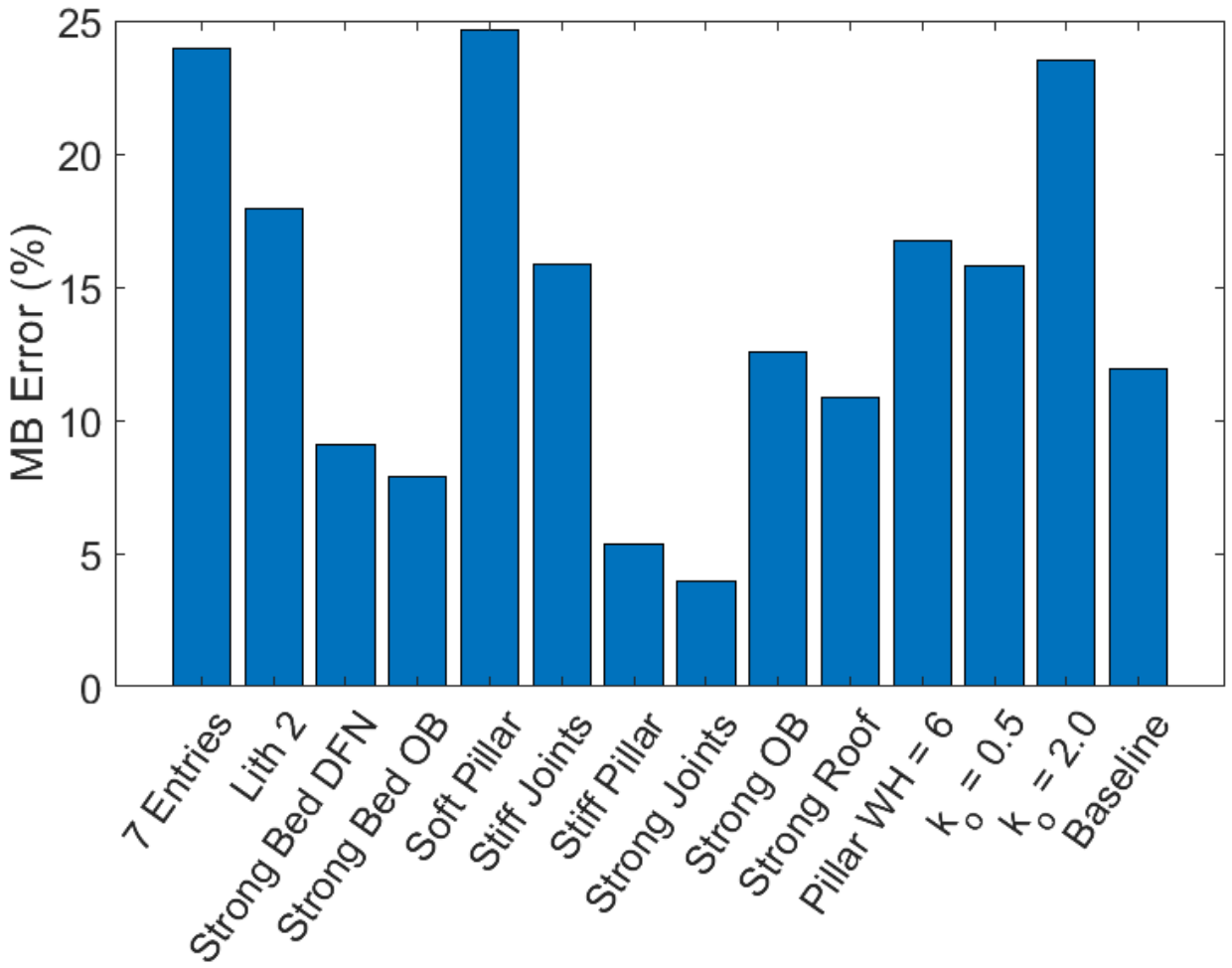

Figure 24: Comparison of the impact of out of plane applied load model inputs on MB predicted pillar strength. Production pillar peak average stresses were compared as a percent change from the MB predicted loads.

As seen in previous modeling efforts in this study (Specific Aim 1), increased strength of the contact between the pillar and the overburden increases the strength of the pillar and approaches the predicted MB strength. Conversely, increased horizontal stress, panel width, and softer pillars decrease the peak strength of the pillar significantly from the baseline condition. Heterogeneity also plays a significant role as indicated by the model results from single strong beds in the DFN and overburden, as well as the Lithology 2 (strong). Note that a homogenously stronger DFN or overburden deviates less from the baseline condition than the heterogeneous strength models. Furthermore, based on the model results, it is clear that TAT overestimates production loads and MB overestimates pillar strength. This generally results in a pillar factor of safety that may still be safe, even though the mechanics of the system have been significantly simplified. A potential case where this could lead to improper design is highlighted by considering a simplified example; a wider panel, where TAT loads are accurate to within 2% (see Figure 23), but the pillar strength has been over-estimated by 24% (see Figure 24), has artificially inflated the factor of safety. This interaction is further explored in Task 4.2. Furthermore, although MB pillar strength accounts for stress gradients within the pillar, a single MB pillar strength cannot capture the potential effects of progressive rib failure (Mohammed et al., 2016) and associated massive roof fall as seen in Task 2.3.

Following the analysis of overburden influence on production pillar loading and strength, the impact on barrier pillar loading was also investigated. Additional model cases featuring an implicit gob model were used to expand the number of panel geometries investigated outside of the initial Task 4.1, and also allow a complete comparison between analytical, continuum, and discontinuum methods. Stress results were extracted and compared to loads predicted by a recommended abutment angle of 21 degrees, in accordance with suggested design parameters from ARMPS and ALPS (Mark, 1992; Mark & Chase, 1997). Expected side-abutment loads following panel extraction for sub-critical and super-critical panel widths were calculated with the following equations:

$$\sigma_{abutment,sub-critical} = \gamma H + \frac{\gamma\left(\frac{H * W_{panel}}{2} - \frac{{W_{panel}}^2}{8tan\beta}\right)}{W_{pillar}}$$

$$\sigma_{abutment,super-critical} = \gamma H + \frac{\gamma\left(\frac{H^2 tan\beta}{2}\right)}{W_{pillar}}$$

where H=entry depth, W=width, γ = overburden specific weight, and β=abutment angle. This predicted side abutment load was compared with average stresses of both left and right barrier pillars from shallow (150 m) models, where full pillar extraction was completed with no contact overlap error in explicit gob models (i.e. model reached an equilibrium solution ratio). As expected, a single abutment angle was significantly inaccurate in predicting the side abutment load transferred to the barrier pillar. The abutment angle error percentage ranged from -34% to 116%, with a mean value of 30%. Interestingly, in almost every model result, the barrier pillar loads for the left and right pillar were remarkably different due to the impact of pillar extraction direction (left to right), as well as the lateral heterogeneity in overburden properties. Explicit gob models highlighting the impact overburden properties have on abutment angle loading on barrier pillars are shown in Figure 25.

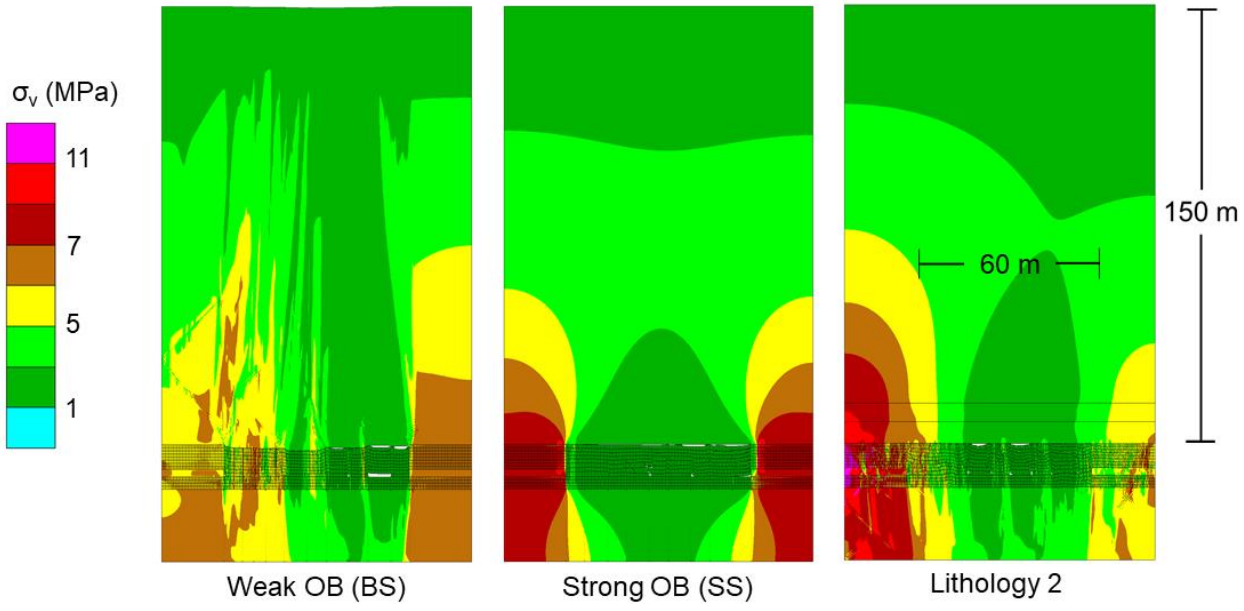

Figure 25: Comparison of the impact that changes in homogeneous overburden (OB) strength, and strong heterogeneous lithology has on abutment angle, as well as barrier pillar and gob loading in explicit gob models.

It is clear that in the Weak Overburden case, the left abutment pillar has shed significant amounts of load onto the gob, as indicated by the vertical stress contours. Unsurprisingly, the Strong Overburden case has maintained a fairly equal stress distribution in both barrier pillars. Interestingly, the left barrier pillar in the stronger heterogeneous stratigraphy (Lithology 2) has more than double the stress in the left barrier pillar than in the right. This is due to the presence of multiple strong layers increasing the abutment angle of the left pillar well beyond the expected range.

The overburden and geometric properties that most significantly impact the difference in abutment side loads between the left and right barrier pillar are shown below in Figure 26. Percent difference between pillar loads were calculated from the average barrier pillar stress at equilibrium using the following equation:

$$\%difference = \frac{abs(\sigma_{yy,LBP} - \sigma_{yy,RBP})}{(\frac{\sigma_{yy,LBP} + \sigma_{yy,RBP}}{2})}$$

where σ_{yy}=average vertical stress, LBP=left barrier pillar, and RBP=right barrier pillar.

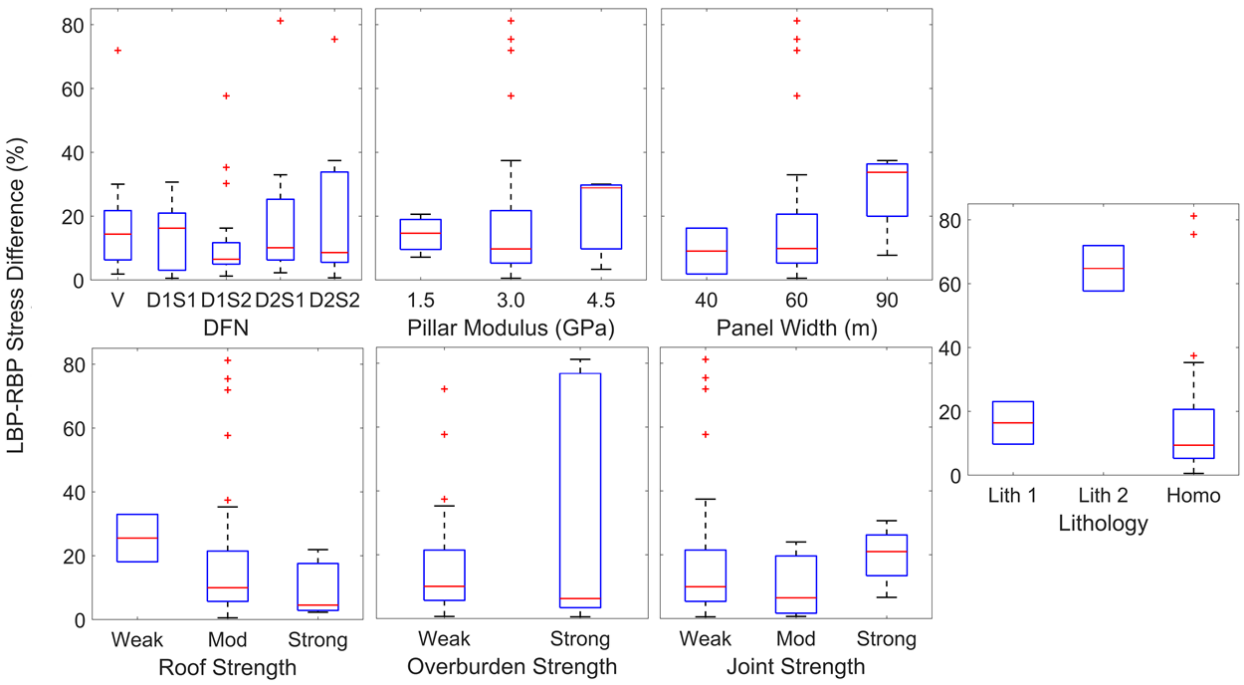

Figure 26: Boxplots showing the impact of overburden and pillar properties, as well as panel geometries on the percent difference in side-abutment load transferred to the left and right barrier pillars. V=voussoir DFN, D1S1=vertical cross joints-seed 1, D1S2=vertical cross joints-seed 2, D2S1=sub-vertical cross joints-seed 1, D2S2=sub-vertical cross joints-seed 2, Mod=moderate, Homo=homogeneous roof and overburden.

Analysis of the results presented above indicate that overburden properties tested, most notably strong lithologies (whether uniformly present in the overburden or only present near the immediate roof), impact side-abutment loading more significantly than panel geometry and pillar properties.

A similar but limited suite of implicit gob models was run based on the cases presented above to analyze the impact on barrier pillar loading, particularly in wider, super-critical panels. Two different overburden

parameters were employed: OB Weak (BS) in Table 8 and those from Task 2.4 (Figure 15b). The parameters from Task 2.4 can be considered to be stronger in comparison to the OB Weak (BS) parameters. In these models, pre-mining stresses were first initialized, followed by replacing the entire panel with the implicit gob elements (equivalent to excavation). The key difference with respect to the panel-scale DEM models is that there were no production pillars and DFN in this case. During the course of the model simulations, vertical stresses and strains in the barrier pillars and the number of yielded zones in the overburden and floor were recorded. The reason for considering two sets of overburden parameters is that the OB Weak (BS) resulted in very low abutment angles and consequently restricted the transfer of stresses onto the barrier pillars. This is illustrated in Figure 27 using vertical stress contours. For this application, it seems that the OB Weak (BS) parameters do not completely capture the overburden mechanics that is observed in the field or it represents a sequence of very weak lithologies. Note that although the DEM models also used the OB Weak (BS) parameters, their behaviors were different, likely due to the presence of the explicit DFN in the immediate roof.

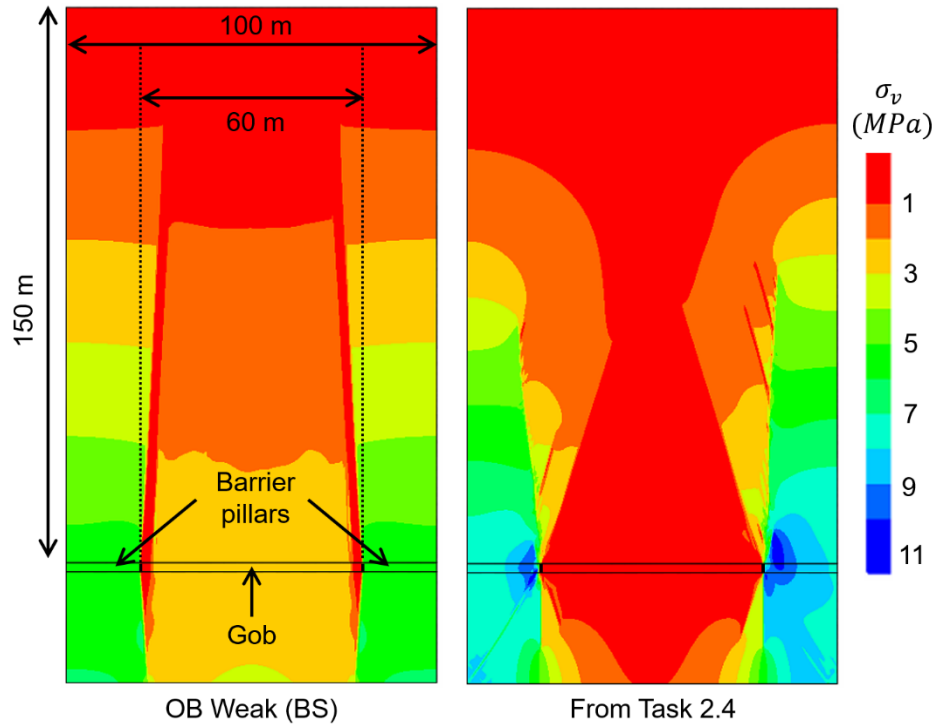

Figure 27: Vertical stress contour in models using overburden properties for OB Weak (BS) and from Task 2.4; k=0.5.

Since the analysis here is focused on barrier pillars only, comparisons were made against the stresses predicted by the abutment angle approach. For this purpose, a 21° abutment angle, based on the recommendation of Mark (1987), was employed in association with the sub-critical panel equation; only for the 132 m panel case (width/depth of 0.88), the super-critical panel equation was used. The average vertical stresses in the barrier pillars as a percentage difference to abutment angle predicted stresses [% Error = 100*(abutment angle predicted stress – Model stress)/(Model stress)] are shown in Figure 28a. A negative % error implies barrier pillar stresses greater than those predicted by the abutment angle approach. The following observations were made based on the model results:

1. Gob stiffness and friction angle of the interface between the pillar and the host rock had minimal impact on the barrier pillar stress.
2. In all models, yielding in the overburden initiated first, followed by yielding in the barrier pillar, if any. The coal pillar yielded significantly only in the 300 m and 450 m depth models using Task 2.4 parameters; the corresponding depths of yield were ~3.5 and ~6.5 m, respectively. In all other cases, the depth of yield was no more than 0.5 m.
3. k_o-ratio had no impact in the OB Weak (BS) models, and had a limited effect in the other models.
4. The stresses in all the OB Weak (BS) models are lower, as the abutment angles in these models are smaller than 21°. On the other hand, the stresses are higher in Task 2.4 parameter models because the abutment angles are larger. The only discrepancy is in the depth model results (green box in Figure 28a) which shows lower stresses than those predicted by the abutment angle approach. A closer look revealed that the pillars in these models were already in their residual state (see point 2) and were consequently carrying less stress.
5. Although the stress difference between the 300 m and 450 m case seems larger in the models with Task 2.4 parameters in Figure 28a, it is actually similar to the difference in the OB Weak case. The difference seems larger since the % error is calculated with respect to the abutment angle predictions, which are different for 300 m and 450 m depth. The change is equivalent to the increase in applied stress along the model top boundary between the 300 m and 450 m depth cases (~3.9 MPa).
6. Panel width had a significant effect on the barrier pillar stresses. The difference is marginal for the 40 m case since the effective stress of overburden being considered for re-distribution is small. As the models with Task 2.4 parameters better capture the abutment loading phenomena, the barrier stress is very close to the predicted value. For the 132 m panel models, it can be seen that the difference is on the order of 80% for OB Weak (BS) model while it is ~-20% for the Task 2.4 parameter model. This large discrepancy is explained by the greater increase in the overburden area per unit change in abutment angle in a super-critical panel in comparison to a sub-critical one (Figure 28b). In other words, the weight of the overburden that is transferred to the barrier pillar increases more in a super-critical panel with changes in the abutment angle. Because the OB Weak (BS) models have low abutment angles, larger discrepancy is naturally expected.
7. In addition to a homogeneous overburden, two other overburden representations were considered - a 2 m thick limestone layer, located at 8 m and 16 m above the coal seam (similar to OB Base and OB + 8 m in Figure 21). For the OB Weak case, the strong bed had a drastic influence, as it increased the abutment angle and raised the pillar stresses from ~5.5 MPa to ~8.8 MPa. This stress magnitude is closer to that obtained in the homogeneous overburden model with Task 2.4 parameters (8.3 MPa). It seems that the presence of a stronger bed within a sequence of weaker lithologies can have a dramatic effect on the stress re-distribution process. Incorporation of the strong bed in the Task 2.4 parameter models had minimal impact and only changed the pillar stresses by 2-4%.

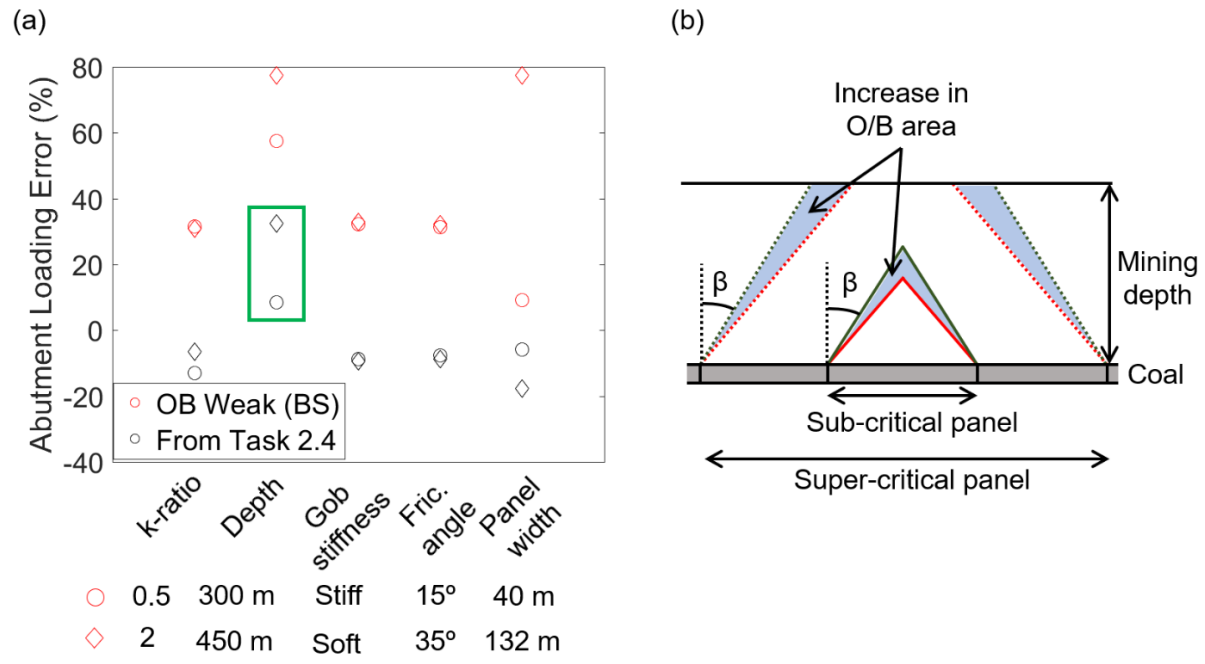

Figure 28: (a) Comparison of the impact of model inputs on abutment angle predicted loads after the implicit gob models achieved mechanical equilibrium. (b) Increase in the area of overburden with change in the abutment angle. β is the abutment angle.

Based on the explicit and implicit gob models, it seems that panel width, mining depth, overburden lithology, and to a lesser extent k_o-ratio are significant inputs requiring further parametric sensitivity analysis.

Task 4.2 – Study Combined Parameter Influences

Based on individual parametric influences on TAT, MB, and abutment side-load error, key parameter combinations were identified in Task 4.1. Table 9 below shows model inputs considered in the parametric sensitivity analysis conducted in Task 4.2.

Table 9: Key parameter combinations identified in Task 4.1 for parametric sensitivity analysis in Task 4.2

Depth/ Loading	DFN Cross Joints	Stress Ratio	Pillar Modulus (GPa)	Lithology	Joint Strength	Pillar W/H	No. Entries	Total Models
150 m	Vertical	0.5	1.50E+09	Baseline (Homo)	Weak	3	5	48
	Sub-Vertical	2	4.50E+09	Strong OB (Homo)	---	6	---	
	---	---	---	Lith 2 (Hetero)	---	---	---	
300m	Vertical	0.5	1.50E+09	Baseline (Homo)	Weak	3	5	112
	Sub-Vertical	2	4.50E+09	Strong OB (Homo)	---	6	7	
	---	---	---	Weak Roof (Soft Pill Only)	---	---	---	
	---	---	---	Lith 2 (Hetero)	---	---	---	
Out-of-Plane	Vertical	0.5	1.50E+09	Baseline (Homo)	Weak	3	5	96

Applied	Sub-Vertical	2	4.50E+09	Strong OB (Homo)	---	6	7	
	---	---	---	Lith 2 (Hetero)	---	---	---	

Again, the impact of overburden properties and model geometry on production pillar TAT and MB error were considered by comparing the TAT error of the 150 m model set and comparing it to the MB error of the same model parameters under applied loading via stress boundary condition (i.e. pushing the pillars to post-peak). In the following analysis, TAT and MB are considered together in terms of a pillar Factor of Safety (FoS) error. A traditional FoS was calculated by dividing the expected MB strength by the expected TAT load, and a model FoS was calculated by dividing the production pillar peak strength from development loads recorded prior to pillar extraction. The range in FoS error for the two pillar W/H cases tested is shown in Figure 29 below.

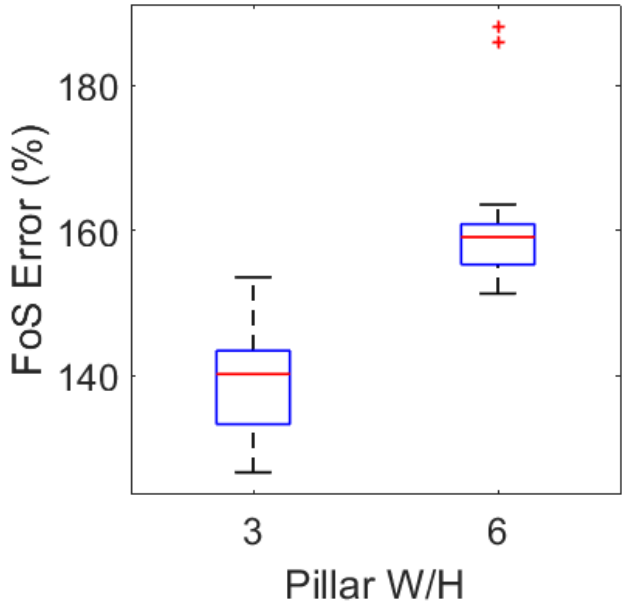

Figure 29: Range of error in FoS when comparing the precent change from "traditional" FoS to a model derived FoS. Traditional FoS for W/H = 3 models was 3.86 and W/H = 6 models was 4.96.

Note the significant over-estimation of FoS by traditional methods when compared to the model results. Specifically, the FoS as determined by the model results range between 1.52-1.97. These findings are also consistent with Tuncay et al. (2020) which found that pillars with higher width to heights (barrier pillars), may require higher FoS than smaller W/H production pillars.

Unsurprisingly, the largest impact on model FoS was controlled by pillar W/H. The most significant overburden parameter was lithology, in which homogenous overburdens increased the absolute pillar FoS, but reversed the marginal decreases associated with sub-vertical joints and higher in-situ stress. Interestingly, the interaction of sub-vertical joints in the explicit DFN and high horizontal stresses resulted in lower FoS for the production pillars in those models. This suggests that even though a single parameter may not have significantly impacted the reliability of TAT or MB, when combined parameters decrease roof self-supporting capacity, pillar FoS decreases. Note that none of the parametric cases tested had a traditionally calculated FoS less than 3.86, confirming the built-in "conservativism" in the state-of-practice MB/TAT methods. However, an over-estimated FoS may provide a false sense of security, particularly

when considering the changing load conditions incurred during depillaring or longwall extraction operations.

Task 4.3 – Synthesize Results

Consideration of the results from the previous sub-sections were used to quantify and summarize the influences of various parameters that have been historically neglected in pillar design. While a universal mathematical relationship between these parameters and panel stability cannot be developed from such a hypothetical study, the knowledge gained has the potential to steer future numerical, laboratory, and in-situ investigation towards the most critical aspects of mine stability that have not fully been explored to date.

The methodical increase in model complexity presented in this study has provided a reliable and repeatable set of results regarding pillar-overburden interaction and its relationship to state-of-practice in underground bituminous coal mines. First, the influence that the roof-pillar contact has on pillar strength and global stability cannot be overstated. The strength and stiffness of the immediate roof contact controls pillar confinement, and therefore, pillar strength and post-peak behavior. This phenomenon was encountered throughout this study at all model scales (i.e. pillar to panel), with inelastic and elastic material, as well as using continuum and discontinuum methods. Future studies investigating pillar strength should explicitly account for this behavior.

Roof self-supporting capacity can be captured by the voussoir beam analog in a multitude of loading conditions. Furthermore, parameters that impact roof stability, such as strong and stiff materials, vertical, low-persistence, widely spaced cross-joints, horizontal and vertical stresses, all impact pillar loading and pillar strength to varying degrees.

This research has shown that pillar design methods that utilize TAT and MB with no consideration of overburden properties are flawed. Safety depends highly on the load transfer between the two systems in order to maintain local and global stability throughout the mine. Fortunately, the overburden parameters that decrease the strength of the pillar also tend to promote stress transfer through the roof (i.e. lower pillar loads), and vice versa. However, the research presented herein has not tested every possible geomining condition and we therefore cannot say with absolute certainty that a condition does not exist where the pillars might simultaneously approach TAT loading and have strength well below that predicted by MB, resulting in dangerously under-designed pillars.

Yield, failure, and functional failure in the roof and pillar have been addressed in this research. At the entry-scale and panel-scale yield can initiate in either the roof or the pillars depending on the state of stress and material properties. A stronger roof is likely to induce additional pillar yield. A rib failure in the pillar can induce large roof failures as seen in Task 2.3, while maintaining pillar functionality from a global perspective. Global failure at the panel scale initiates in the pillar, but the peak strength and post-peak behavior are governed by the loading conditions as dictated by the roof and floor. So the question of which component is critical to system stability can be answered when the scale of the system and the material strength contrast between the components are well-defined.

4.0 Summary of Findings

<u>Specific Aim 1 – Establish a Numerical Representation for Pillars</u>

An improved rock yield criterion, termed as the progressive S-shaped yield criterion, was shown to be capable of reproducing the damage evolution in a coal pillar rib. Specifically, displacements and stresses as measured in an Australian coal mine were reproduced in the model for different locations of the longwall face. The criterion was also used to conduct pillar compression tests and peak strengths for W/H of 2, 4, and 6, as predicted by the empirical Mark-Bieniawski equation, were replicated. The models also exhibited a transition from brittle to pseudo-ductile behavior with increase in the W/H ratio – a behavior that is supported by previous numerical studies (Esterhuizen et al., 2010) as well as laboratory testing (Das, 1986). Overall, a continuum representation of coalmasses using the progressive S-shaped criterion was found to be promising in capturing coal pillar behavior. Interfaces were subsequently included in a simulated compression test and the peak strength was found to reduce by 21%. This implies that pillars having a weaker contact with the host material (e.g. clay infilled) can have reduced strengths and greater chances of failure.

Specific Aim 2 – Establish an Approach for Numerical Representation of Roof and Overburden Mechanics

A wide range of geomining conditions that accurately account for the discontinuous and anisotropic nature of coal-measure rock have been successfully represented using the DEM approach. Development and analysis of voussoir DFN single entry models (Task 2.1) allowed for confirmation of solution methodologies and bolt parameters prior to investigating a wide range of geomining conditions. Furthermore, the applicability of the voussoir beam analog to the modeling of jointed roofs was confirmed. Standard bolting was found to have a limited impact on self-stability, particularly in voussoir entry models with low (0.5) and high (2.0) horizontal stress ratios.

Models investigating roof stability for a wide range of plausible geomining conditions (Task 2.2) were confirmed to behave realistically by using empirical and analytical systems such as CMRR and ARBS. Stability was classified using displacement and velocity of the immediate roof, as well as the capacity for voussoir arching. Through statistical analysis of over 10,000 unique numerical models, the most significant controls on roof stability were identified. Interestingly, they matched sensitivities governing predicted stability in the empirical ARBS system.

Major considerations for state-of-practice emerged from roof stability models, such as, special considerations when accounting for horizontal stress ratios, the presence of closely-spaced *sub-vertical joints decreasing roof stability and increasing variable pillar loading in single-entries*, augmenting the observational method utilized in rockmass rating systems using numerical models, and approaching a both probabilistic and factor of safety based roof design and roof support optimization. Furthermore, the mechanical behavior of the immediate roof was thoroughly investigated, and through BLR, the significant combinations of model inputs were identified.

A wide range of properties capturing multiple geomining conditions were confirmed as realistic for future academic and industry applications. *Roof stability mechanics in elastic pillar models were first and foremost governed by the state of stress.* At low depths, most combinations of roof parameters were stable; however, low horizontal stresses and very weak material properties could not create and maintain enough self-support through voussoir arching. *As depth increases, the self-supporting capacity of the roof material, is increasingly controlled by the stiffness and strength of intact materials, presence of anisotropic strength via SUBI constitutive models, and DFN geometric properties.* The explicit joint strengths and bedding thicknesses tested marginally impacted roof stability at all entry depths.

Calibrated pillar models have shown that the interaction between roof and pillar significantly effects pillar loading, which in turn impacts the stability of a single-entry. The stability of the entry and the types of failures that occur depend largely on the roof conditions for shallow entries, the contrast between roof and pillar strength in moderate depth entries, and the horizontal stress conditions in deeper entries. *The associated effects on load transfer between the overburden and pillars is predominantly governed by pillar properties and stress state. However, the impact of overburden properties can cause up to 35% error in pillar load and strength calculations that do not consider those properties.* Furthermore, state-of-practice pillar strength determination does not account explicitly account for rib failure, which contributes to total entry failure by increasing the pillar loads and the entry span, increasing the likelihood of roof fall or pillar failure over time.

***Associated Research Question*:** What effect does horizontal stress, horizontal bedding, and vertical joints play in overburden stability?

Research Finding: Horizontal stresses, horizontal bedding, and vertical joints all contribute to local roof stability, particularly at greater depths, by controlling the magnitude and distribution of horizontal stresses through the immediate roof. If horizontal stresses are high (e.g. k_o=2.0) and subvertical joints are present, or intact material is sufficiently weak, roof stability will decrease significantly. Additionally, if horizontal stresses are too low (e.g. k_o=0.5) and vertical or sub-vertical joints are present, roof stability will decrease due to lack of voussoir arching through the immediate roof.

Associated Research Question: Do coal pillars fail or yield prior to overburden failure or does the overburden failure cause pillar failure?

Research Finding: The answer to this question is heavily dependent on the state of stress around a given entry, as well as the strength and stiffness contrasts of the roof and pillar. *Material Yield* can initiate in either the roof or the pillar and roof depending on the aforementioned properties. However, in the model cases tested, *total entry failure* (i.e. functional failure of the pillar ribs, functional failure of the entire pillar, and roof collapse) initiates in the pillars. Once the pillar fails and sheds the initial load, roof properties and model loading conditions heavily influence the post-peak behavior of the pillar. None of the model cases tested in Task 2.3 identified a set of conditions where complete failure of the overburden and roof caused a subsequent pillar failure.

Associated Research Question: Do coal pillars act to reinforce the overburden, and how?

Research Finding: It is known that coal pillars reinforce the overburden by providing standing support for vertical dead-loads. This study has identified that locally and globally, pillars act as abutment support for the immediate roof, allowing for sufficient horizontal stress transfer across entries, enabling the immediate roof to engage self-support and take on surcharge loading from the back.

<u>Specific Aim 3 – Develop Baseline Models to Test Illustrative Conceptual Model Cases</u>

The models run for this task were based primarily on the thought experiments of Frith and Reed (2018). It was found that under a massive roof, when the k_o-ratio was low and the vertical joints along the barrier pillars were weak, pillars underwent extensive rib damage due to slippage along the joints. When the k_o-ratio or the joint strength property was raised, frictional forces along the vertical joints were mobilized and allowed for effective stress transfer to the barriers, thereby stabilizing the isolated pillar. No pillar damage or stress transfer issue was noted in the shallower depth models due to the low associated vertical stresses. These simple models highlight the importance of understanding *the geology (large-scale fractures) at the*

site and the in-situ stress conditions when assessing/designing coal pillars. A deeper, rigid overburden model was also run and in this case, a de-stressed arch formed over the isolated pillar; consequently, the isolated pillar did not carry much load and the stresses were channeled to the barriers. This means that *a low FS pillar under a rigid (or very stiff) overburden will not fail unless the barrier pillars fail.*

Similar models were also run with two different stratigraphies corresponding to stiff and a soft immediate roof. In the unjointed case (no vertical joints along barrier) with low k_o-ratio, the pillar with a soft immediate roof layer was fully yielded at model equilibrium and carried low stresses, while that with the stiff immediate roof layer was stable. The presence of a stiff bed limited the flexure of the immediate roof and thereby stabilized the isolated pillar. When the pillar width in the soft immediate roof model was increased, it stabilized, as wider pillars have greater peak strength. This indicates that *the proximity of a stiff bed to the coal seam can significantly alter the pillar integrity* and a wider pillar might be required under weak immediate roofs.

***Associated Research Question*:** What effect does horizontal stress, horizontal bedding, and vertical joints play in overburden stability?

Research Finding: Horizontal stresses and vertical joint properties both contribute to global stability by controlling the magnitude of frictional force developing along the joints and possible slippage. Horizontal stiff beds in immediate roof can limit flexure, transfer load to the barriers and ensure stability of isolated pillars.

Specific Aim 4 – Quantify Parametric Interactions and Influences on Overburden and Pillar Stability

A parametric analysis of panel-scale de-pillaring activities was conducted using both explicit and implicit gob representations. The explicit gob models found *TAT to consistently overestimate the stresses within the production pillars*. The analysis was conducted with multiple overburden properties and input parameters such as panel width, roof lithology, explicit DFN geometry, pillar properties, in situ stress ratio, and mining depth. Changes in depth and pillar W/H had the most significant impact on TAT error, with increasing depth and decreasing pillar W/H and panel width resulting in greater error. The overburden properties that most significantly impact TAT were decreases in roof strength and increased horizontal stress, which increased TAT error. Assuming overburden dead-loads can overestimate production pillar loads by up to 50%.

Pushing pillars to post-peak behavior by applying a stress boundary condition to the top of the model (simulating out of plane loading by de-pillaring) allowed for similar analysis of model geometry and overburden properties on MB pillar strength predictions. Panel width and pillar stiffness had the largest impact on MB error, but high horizontal stress and explicit strength and stiffness of the overburden and immediate roof impacts also had significant impacts. Interestingly, a heterogeneous but generally strong overburden with a strong immediate roof (Lithology 2) increased the MB error, while a homogeneously strong roof and overburden, or the presence of a single strong bed in the roof or overburden, led to pillar strength results closer to the MB pillar strength estimation. This indicates that accurately capturing heterogeneous stratigraphy is critical in estimating production pillar strength. Ultimately, it was found that the MB pillar strength equation can over-estimate production pillar strength by up to 25%.

Abutment side-loading of barrier pillars was investigated from the same set of model results and the scope of investigation was further expanded with the development of implicit gob models. The percent error in abutment side load ranged from -34% to 116%, with a mean value of 30% (abutment angle calculations

tend to overestimate abutment side load) in the implicit gob models. Explicit gob models found a similar range in error (-20% to 80%). Panel width, roof lithology and mining depth were identified as important parameters from the implicit models. Most notably, the explicit gob model results showed significant differences in abutment loads for the left and right barrier pillars due to the influence of mining direction and heterogeneity in the explicit gob that the implicit gob model could not represent. Also, changes in overburden heterogeneity and strength induced up to 80% difference between left and right barrier pillar abutment loads. Furthermore, the DFN geometry had a non-negligible impact on the mean difference between left and right barrier pillar loads. One can imagine a case where a prominent sub-vertical joint set is oriented slightly towards either pillar, significantly impacting the load transfer between the overburden and pillars.

Finally, a parametric analysis of geometric, loading, and overburden properties critical to controlling TAT and MB error was conducted using explicit gob models, and the results were interpreted with respect to pillar FoS. Results indicated that, in particular, *subvertical fractures, coupled with high horizontal stresses decreased production pillar FoS relative to other parametric cases. Heterogeneous roof stratigraphy also decreased FoS. Roof displacement was compared to pillar loading, and it was determined that in total entry and global mine failure, the pillars fail first, except in cases with extremely weak roofs.*

Associated Research Question: Can pillar strength be estimated from tributary area loading at collapse and are coal pillar capacities being overestimated in conventional tributary area design evaluations?

Research Finding: The TAT approach for loading estimation and the MB approach for pillar strength, were both found to be inaccurate. Typically, it appears that the magnitude by which TAT overestimates pillar loads is always less than the amount by which MB pillar strengths are overestimated under the geomining and loading conditions tested in this study. Accordingly, traditional FoS estimates are much higher than model FoS estimates, but by a consistent amount (120-180%) indicating that there may be a reasonable, simplified adjustment to traditional FoS estimates that could be made; it should be noted that W/H was found to directly influence the error in the traditional FoS estimates, so any such correction would need to account for this. Regardless, the fact that traditional FoS calculations are not based on a complete assessment of the system mechanics means that the potential exists for catastrophic failures to occur in unique circumstances where the errors in pillar stress and strength estimates are not similar.

Associated Research Question: What effect does the in-situ vertical stress have on pillar response? How does the in-situ stress effect the mining-induced compression required to produce pillar yielding and failure?

Research Finding: The effect of vertical stress on pillar response has previously been understood to be a direct, linear relationship. This study indicates that this assumption is far too simplistic to capture the full spectrum of pillar response to loading. Outside of overburden properties, a significant effect on peak pillar strength was identified based on in-situ vertical stress and incremental loading. If the in-situ load was moderate (300 m), the left-most production pillar reached a peak strength of 10.5 MPa at an average vertical strain of 2.1 mstrain (MB error = 35%). If in-situ loading was high (450 m), the left-most production pillar reached a peak strength of 12.5 MPa at an average vertical strain of 1.1 mstrain (MB error = 12%). If load is increased slowly from a low (150 m) in-situ state of stress, the left-most production pillar reached a peak strength of 12.3 MPa at an average vertical strain of 3.5 mstrain (MB error = 12%).

5.0 Dissemination Efforts & Highlights

The findings of this research have been presented at multiple conferences and published in conference proceedings, as well as journal publications. The conference paper Abousleiman et al. (2019) was selected as one of "The Best of Ground Control 2019" talks from the International Conference on Ground Control in Mining.

Record of Publications

Conference Papers

- Abousleiman, R., Walton, G., & Sinha, S. (2019) Understanding Roof Deformation Mechanics and Parametric Sensitivities of Coal Mine Entries Using the Discrete Element Method. *2019 International Conference on Ground Control in Mining*. Morgantown, WV.
- Abousleiman, R., Walton, G., & Sinha, S. (2020) Expanding Understanding of the Voussoir Beam Analog in Flat Roof Excavations Using the Discrete Element Method. 54th *American Rock Mechanic/Geomechanics Symposium.* Submitted for review March 2020.

Journal Papers/Technical Notes

- Sinha, S., & Walton, G. (2020) Modeling Behaviors of a Coal Pillar Rib using the Progressive S-shaped Yield Criterion. *Journal of Rock Mechanics and Geotechnical Engineering*. https://doi.org/10.1016/j.jrmge.2019.12.002
- Abousleiman, R., Walton, G., & Sinha, S. (2020) Understanding Roof Deformation Mechanics and Parametric Sensitivities of Coal Mine Entries Using the Discrete Element Method. *International Journal of Mining Science & Technology.*

6.0 Conclusions and Impact Assessment

The research presented herein represents a critical step forward in understanding the mechanics of underground stability in bituminous coal mining. Overburden properties that have long been ignored in mine design have been considered, and their effects are practically significant. Continuing to design mines using existing empirical and analytical methods will not improve worker safety. While total mine failures, such as those that occurred at Crandall Canyon and Coalbrook, were the major motivation for this study, smaller local failures continue to injure and kill miners as well. This research presents a unique approach to represent the mechanical interaction of all underground components to approach a design methodology that can account for the complexity of real scenarios, while still being practically applicable.

Geometric conditions (e.g. panel width, pillar W/H, and depth to entry), loading conditions (e.g. in-situ stress ratio), overburden properties (e.g. DFN, material strength and stiffness, discontinuity strength, and heterogeneous stratigraphies), and pillar properties (e.g. W/H and stiffness) all have significant effects on pillar loading and pillar response. Through BLR, the critical parameter governing self-supporting capacity of the roof was identified as the state of stress, as governed by the depth to entry. At shallow depths, self-stability is almost guaranteed, but with increasing depth, the self-supporting capacity of the roof material is increasingly controlled by the stiffness and strength of intact materials, the presence of anisotropic weakness planes (as modeled via the SUBI constitutive model), and the presence of sub-vertical joints.

Critical inputs governing roof stability analyzed with the calibrated coal pillar model in single entries indicated that total entry failure generally initiates in the pillars, except in extremely weak roof cases. However, intact material properties and in-situ stress ratio significantly influenced the post-peak behavior

of the pillars. Preliminary analyses of pillar loading and strength in single entries indicated that TAT and MB were not accurate in the case of an infinite series of entries (as modeled using a single entry and symmetry condition in this study). These errors, in addition to side-abutment loading of barrier pillars, were explored at the panel scale. Results indicated that production pillar FoS and barrier pillar abutment loads (post panel extraction) were most significantly impacted by panel geometry and pillar properties (e.g. depth, panel width, pillar stiffness, pillar W/H). However, in-situ stresses and overburden properties had significant impacts as well. In particular, heterogeneous stratigraphy and strength, stiffness, and anisotropy of the overburden violate the CHILE assumptions utilized in common modeling methods and result in significant errors when left unaccounted for. Arguably, the most critical overburden parameter for consideration in current pillar design is the strength of the contact between the pillar and the immediate roof. This contact directly controls the stress transfer between the roof and overburden, and ultimately, pillar strength.

The immediate impact of this research is to provide a quantitative sense of the degree of adjustments to state-of-practice design calculations that may be needed when mine designers assess roof stability and pillar loading, respectively. The confirmation of realistic roof behavior and comparability to empirical rockmass rating systems can help engineers prepare for roof conditions and adjust support accordingly. For example, if a given mine or company has a standard practice for classifying the roof and back to dictate support requirements, and the uncertainty surrounding roof conditions is high (i.e. pinch-outs, strength values, moisture sensitivity, clay seams, faulting or changes in joint distribution), then numerical models can be used to anticipate combinations of parameters that have not been observed and assess support effectiveness. The example cases demonstrating the limitations of using TAT and MB to assess pillar FoS in various overburden conditions will allow engineers to consider where larger pillars may be needed during production, or where additional mobile roof support is required during depillaring operations, based on roof and loading conditions.

7.0 Recommendations for Future Work

Specific Aim 1

1) Utilize the progressive S-shaped criterion to capture novel laboratory compression test (unconfined and triaxial) data for different coal types. This can constrain thresholds for crack initiation and crack damage and establish ranges for practical use.
2) Voronoi tessellations (polygonal blocks) or Trigons (triangular blocks) can be incorporated in the coal pillar that will allow for explicit fracturing and separation of the rib. As this approach has been shown to reproduce the rock support interaction mechanism (Sinha and Walton, 2019; Walton and Sinha, 2020), such a representation along with a DEM overburden will allow assessing support needs under various geological conditions as well as improve our understanding of how (or if) pillar support might affect its interaction with the overburden.

Specific Aim 2

1) Investigate the applicability of a factor of safety/probability-based roof support design method that incorporates the support capacity of multiple support types, potentially based on voussoir mechanics. Model different conditions with the goal of optimizing roof support layouts, particularly its application in high horizontal stress regimes.

2) Incorporate voussoir mechanics into recommendations for critical displacement thresholds for comparison against monitoring data to assess changes in stability over time for a given entry or intersection.
3) Utilize the hydro-mechanically coupled models to simulate groundwater impacts and deterioration of roof conditions due to the presence of moisture-sensitive rock types.
4) Model heterogeneous roof conditions in the context of individual entries (i.e. heterogeneous beds and associated joint properties).
5) Investigate the full suite of roof conditions tested in Task 2.2 on the calibrated pillar single-entry models in Task 2.3.

Specific Aim 3

1) While simulating the different roof layers using an elastic anisotropic constitutive model yielded some interesting results, this analysis could be repeated using inelastic roof layers. This was not attempted, as there is currently no inelastic constitutive model in UDEC that also allows assignment of anisotropic elastic properties (i.e. a transversely isotropic inelastic model).

Specific Aim 4

1) Increase the number of roof conditions tested to the consider the full Task 2.2 suite and determine if practical quantitative adjustments to TAT and MB based on overburden properties and local pillar-roof contact strengths is possible.
2) Utilize the modeling results developed to investigate the accuracy of simplified model-based design applications such as ARMPS and LaModel in specific cases.
3) Model a wider variety of support systems so that weak roof impacts on pillar loading can be further confirmed as realistic.

General

1) Further study is required to identify how the hardening behavior of gob can be better captured using DEM. It seems that the implicit representation of gob is more effective in reproducing the hyperbolic nature. There might be benefits in testing the Voronoi/Trigon representation within the first few immediate roof layers.
2) With increased computational capability, limited portions of this study could be repeated in three-dimensions.

8.0 References

Alejano, L. R., Ramírez-Oyanguren, P., & Taboada, J. (1999). FDM predictive methodology for subsidence due to flat and inclined coal seam mining. *International Journal of Rock Mechanics and Mining Sciences, 36*(4), 475-91.

Bahrani, N., & Hadjigeorgiou, J. (2017). Explicit reinforcement models for fully-grouted rebar rock bolts. *Journal of Rock Mechanics and Geotechnical Engineering, 9*(2), 267–280. https://doi.org/10.1016/j.jrmge.2016.07.006

Colwell, M. G. (2006). *A study of the mechanics of coal mine rib deformation and rib support as a basis for engineering design*. Ph.D. thesis, University of Queensland, Australia.

Das, M. N. (1986). Influence of width/height ratio on post-failure behaviour of coal. *International Journal of Mining and Geological Engineering, 4*(1), 79-87.

Diederichs, M. S. (2003). Rock fracture and collapse under low confinement conditions. *Rock Mechanics and Rock Engineering*, *35*(5), 339-381.

Diederichs, M. S. (2007). The 2003 geotechnical colloquium: Mechanistic interpretation and practical application of damage and spalling prediction criteria for deep tunneling. *Canadian Geotechnical Journal*, *44*(9), 1082–1116.

Diederichs, M. S., & Kaiser, P. K. (1999). Stability of large excavations in laminated hard rock masses: The voussoir analogue revisited. *International Journal of Rock Mechanics and Mining Sciences*, *36*(1), 97–117. https://doi.org/10.1016/S0148-9062(98)00180-6

Esterhuizen, E., Mark, C., & Murphy, M. M. (2010). Numerical model calibration for simulation coal pillars, gob and overburden response. Proceeding of the *29th International Conference on Ground Control in Mining*, Morgantown, WV.

Esterhuizen, G. S., & Barczak, T. M. (2006). Development of ground response curves for longwall tailgate support design. Proceedings of the *41st U.S. Rock Mechanics Symposium*, Golden, Colorado, 1–10.

Evans, W. H. (1941). The Strength of Undermined Strata. *American Institute of Mining and Metallurgical Engineers*, *50*, 475–500.

Frith, R., & Reed, G. (2018). Coal pillar design when considered a reinforcement problem rather than a suspension problem. *International Journal of Mining Science and Technology*, *28*(1), 11–19. https://doi.org/10.1016/J.IJMST.2017.11.013

Hajiabdolmajid, V., Kaiser, P. K., & Martin, C. D. (2002). Modelling brittle failure of rock. *International Journal of Rock Mechanics and Mining Sciences*, *39*(6), 731–341.

Hudson, J. A., & Harrison, J. P. (1997). *Engineering Rock Mechanics: An Introduction to the Principles.* Amsterdam, Netherlands: Elsevier, pp. 456.

Iannacchione, A. T. (1990). The effects of roof and floor interface slip on coal pillar behavior. Proceedings of the *31st US rock mechanics Symposium*. Rotterdam: Balkema, 53–60.

Jing, L. (2003). A review of techniques, advances and outstanding issues in numerical modelling for rock mechanics and rock engineering. *International Journal of Rock Mechanics and Mining Sciences*, *40*(3), 283–353. https://doi.org/10.1016/S1365-1609(03)00013-3

Kaiser, P. K., Diederichs, M. S., Martin, D., Sharp, J., & Steiner, W. (2000). Invited keynote: underground works in hard rock tunnelling and mining. Proceedings of *GeoEng2000*, Melbourne, 841–937.

Kaiser, P. K., & Kim, B. (2008). Rock mechanics advances for underground construction in civil engineering and mining. Proceedings of *KRMS* 2008, Seoul, 3–16.

Kaiser, P. K., McCreath, D., & Tannant, D. (1995). *Canadian Rockburst Support Handbook*. Geomechanics Research Center and CAMIRO.

Kim, B., Walton, G., Larson, M. K., & Berry, S. (2018). Experimental study of the confinement-dependent characteristics of a Utah coal considering the anisotropy of cleats. *International Journal of Rock Mechanics and Mining Sciences*, *105*, 182-191.

Lekhnitskii, S. G. (1981). *Theory of Elasticity of an Anisotropic Body*. Moscow: Mir Publishers.

Majdi, A., Hassani, F. P., & Nasiri, M. Y. (2012). Prediction of the height of destressed zone above the mined panel roof in longwall coal mining. *International Journal of Coal Geology*, *98*, 62–72. https://doi.org/10.1016/j.coal.2012.04.005.

Mark, C. (1987). *Analysis of Longwall Pillar Stability. Ph.D.* Dissertation, The Pennsylvania State University.

Mark, C. (2015). Design of Roof Bolt Systems. In *New Technology for Coal Mine Roof Support, Proceedings, NIOSH Open Industry Briefing* (pp. 111–132).

Mark, C., Pappas, D. M., & Barczak, T. M. (2011). Current trends in reducing ground fall accidents in US coal mines. *Mining Engineering*, *63*(1), 60–65.

Mark, C., Molinda, G. M., & Dolinar, D. R. (2001). Analysis of roof bolt systems. *Coal International*, *253*(1), 28–34.

Martin, C. D., & Chandler, N. A. (1994). The progressive fracture of Lac Du Bonnet granite. *International Journal of Rock Mechanics and Mining Sciences and Geomechanical Abstracts*, *31*(6), 643-659.

Mishra, B., & Nie, D. (2013). Experimental investigation of the effect of changes in control models on the post-failure behavior of coal and coal measures rock. *International Journal of Rock Mechanics and Mining Sciences*, *60*, 363-369.

Mohamed, K. M., Tulu, I. B., & Murphy, M. M. (2016). Numerical model calibration for simulating coal ribs. Proceedings of the *Society for Mining, Metallurgy and Exploration Inc Annual Conference*, Pheonix, Arizona.

Molinda, G., & Mark, C. (2010). Ground failures in coal mines with weak roof. *Electronic Journal of Geotechnical Engineering*, *15 F*, 1–42.

Molinda, G. M., & Mark, C. (1994). The coal mine roof rating (CMRR) a practical rock mass classification for coal mines. In *12th International Conference on Ground Control in Mining* (pp. 92–103). US Burea of Mines and Reclamation.

Poeck, E. C. (2016). *Analyzing the potential for unstable mine failures with the calculation of released energy in numerical models*. Ph.D. Dissertation, Colorado School of Mines.

Reed, G., Mctyer, K., & Frith, R. (2016). An assessment of coal pillar system stability criteria based on a mechanistic evaluation of the interaction between coal pillars and the overburden. In *35th International Conference on Ground Control in Mining 2016* (pp. 146–152). Society for Mining, Metallurgy and Exploration. https://doi.org/10.1016/j.ijmst.2016.09.031

Sinha, S., & Walton, G. (2018). A progressive S-shaped yield criterion and its application to the study of rock pillar behavior. *International Journal of Rock Mechanics and Mining Sciences*, *105*, 98-109.

Sinha, S., & Walton, G. (2019). Understanding continuum and discontinuum models of rock-support interaction for excavations undergoing stress-induced spalling. *International Journal of Rock Mechanics and Mining Sciences*, *123*, 104089.

Sinha, S., & Walton, G. (2020). Modeling behaviors of a coal pillar rib using the progressive s-shaped yield criterion. *Journal of Rock Mechanics and Geotechnical Engineering*. https://doi.org/10.1016/j.jrmge.2019.12.002

Starfield, A. M., & Cundall, P. A. (1988). Towards a methodology for rock mechanics modelling. *International Journal of Rock Mechanics and Mining Sciences & Geomechanics Abstracts*, *25*(3), 99-106.

Tuncay, D., Tulu, I. B., & Klemetti, T. (2020). Analysis of ARMPS2010 database with LaModel and an updated abutment angle equation. *International Journal of Mining Science and Technology*, *30*, 111-118. https://doi.org/10.1016/j.ijmst.2019.12.020

Vlachopoulos, N., & Diederichs, M. S. (2009). Improved longitudinal displacement profiles for convergence confinement analysis of deep tunnels. *Rock Mechanics and Rock Engineering*, *42*, 131–146. https://doi.org/10.1007/s00603-009-0176-4.

Walton, G., & Sinha, S. (2020). Advances in Bonded Block Modeling. Proceedings of *Bergmekanikdagen*, Swedish Rock Engineering Association, Sweden.